Draft version December 19, 2023
Typeset using LaTeX **twocolumn** style in AASTeX631

Multi-Point Observations of the Dynamics at an ICME Sheath-Ejecta Boundary

Matti Ala-Lahti [1,2], Tuija I. Pulkkinen [1], Julia Ruohotie [2], Mojtaba Akhavan-Tafti [1], Simon W. Good [2] and Emilia K. J. Kilpua [2]

[1] *Department of Climate and Space Sciences and Engineering, University of Michigan, Ann Arbor, Michigan 48109, USA*
[2] *Department of Physics, University of Helsinki, Finland*

Submitted to ApJ

ABSTRACT

The radial evolution of interplanetary coronal mass ejections (ICMEs) is dependent on their interaction with the ambient medium which causes ICME erosion and affects their geoefficiency. Here, an ICME front boundary, which separates the confined ejecta from the mixed, interacted sheath-ejecta plasma upstream, is analyzed in a multi-point study examining the ICME at 1 AU on 20 April 2020. A bifurcated current sheet**, highly filamented currents and a** two-sided jet were observed at the boundary**. The two-sided jet, which was recorded for the first time for a magnetic shear angle** $< 40^\circ$, implies multiple (patchy) reconnection sites associated with the ICME erosion. The reconnection exhaust exhibited fine structure including multi-step magnetic field rotation and localized structures that were measured only by separate Cluster spacecraft **with the mission inter-spacecraft separation of** $0.4-1.6\,\mathrm{R_E}$. The mixed plasma upstream of the boundary with a precursor at 0.8 AU lacked coherency at 1 AU and exhibited substantial variations of southward magnetic fields over radial (transverse) distances of $41-237\,\mathrm{R_E}$ ($114\,\mathrm{R_E}$). This incoherence demonstrates the need for continuous (sub)second resolution plasma and field measurements at multiple locations in the solar wind to adequately address the spatio-temporal structure of ICMEs and to produce accurate space weather predictions.

Keywords: Solar coronal mass ejections (310) — Interplanetary magnetic fields (824) — Solar magnetic reconnection (1504) — Solar wind (1534)

1. INTRODUCTION

Solar activity regularly results in vast transient eruptions of plasma and magnetic field from the Sun's corona known as coronal mass ejections (CMEs). Their interplanetary counterparts, ICMEs, have properties distinct from the solar wind such as a low-β plasma, coherent rotation of the magnetic field at large scales, low proton temperature, counter-streaming electrons, and elevated amounts of high charge state heavy ions (Zurbuchen & Richardson 2006; Kilpua et al. 2017). ICMEs displaying a strong magnetic field with a particularly coherent rotation are classified as magnetic clouds. They resemble a flux rope configuration, which has made them a specific interest of research**, with many studies having focused** on their radial evolution in interplanetary space (e.g., Good et al. 2015, 2018, 2020; Manchester et al. 2017; Al-Haddad et al. 2019; Salman et al. 2020; Palmerio et al. 2021; Scolini et al. 2021). ICMEs may exhibit a layered structure which consists of the magnetic cloud itself and preceding and following non-cloud-like ejecta signatures (Kilpua et al. 2013). For example, coronal loops can pile up in front of erupting plasma which builds a so-called front region of an ICME. Such loops appear as bright regions in white-light images (Kilpua et al. 2013; Vourlidas et al. 2013).

ICMEs often travel with supermagnetosonic speeds relative to the ambient solar wind, which results in the formation of a shock upstream of the ejecta. The shocked solar wind plasma deflects around the magnetically confined ejecta forming a turbulent high-β plasma

Corresponding author: Matti Ala-Lahti
amatti@umich.edu

sheath region. ICME sheaths differ from their planetary counterparts due to the expanding nature ICMEs have in interplanetary space. This causes relatively small deflection speeds and the accretion of plasma in front of the ICME nose (Siscoe & Odstrcil 2008).

Many ICMEs interact with their sheath regions. Under favorable conditions, magnetic reconnection connects the topologically separate sheath and ICME plasmas with each other at the ICME front boundary. At the boundary, asymmetric inflow conditions control reconnection, as relatively hot and dense sheath plasma couples with the tenuous low-β ejecta plasma. As a consequence, the ejecta experiences magnetic flux erosion and forms a boundary layer, where sheath and ejecta plasmas are mixed (Wei et al. 2003; Dasso et al. 2006; Ruffenach et al. 2012, 2015; Lavraud et al. 2014). This so-called mixing layer typically features properties of magnetic reconnection such as high proton temperature, high proton density and high-β **plasma**, i.e. so-called "three-high state" plasma. The three-high state coincides with abrupt large magnetic field rotations and an intensity drop. ICME erosion is a frequent process and on average 42% of the azimuthal flux of magnetic clouds has eroded away when they are observed at 1 AU (Ruffenach et al. 2015). The mixing layer is ultimately considered as part of the sheath region**, and has not typically been** distinguished as a separate region in statistical studies (e.g., Palmerio et al. 2016; Ala-Lahti et al. 2018; Kilpua et al. 2019).

A magnetic reconnection outflow region in interplanetary space is often characterized by a magnetic field rotation that happens in two steps (e.g., Phan et al. 2006, 2020; Gosling et al. 2005, 2006a,b; Gosling & Szabo 2008; Huttunen et al. 2007, 2008; Eriksson et al. 2009, 2022; Mistry et al. 2015b, 2016; Eastwood et al. 2021; Vörös et al. 2021) as predicted by the original Petschek reconnection model (Petschek 1964). This profile of a bifurcated current sheet is also typically associated with a forward-reverse slow-mode wave-pair, which propagates away from the exhaust axis and bounds a region of decreased magnetic field strength and increased plasma density that coincides with outflow jets (Gosling et al. 2005, 2006a,b; Phan et al. 2006). The detailed exhaust structure can become more complex when asymmetries between reconnecting plasmas are present (Semenov et al. 1983; Heyn et al. 1985; Owen et al. 2021). Compared to symmetrical inflow conditions with a merged Alfvén wave and slow-mode wave/shock-pair bounding the exhaust region, the asymmetric case can introduce a multi-layered outflow region due to the waves and discontinuities separating from each other. The importance of this picture for solar wind reconnection has been recently highlighted by Owen et al. (2021) (see also Lin & Lee 1993; Teh et al. 2009). Reconnection can furthermore drive non-Petschek-type discontinuities in the inflow regions, which can contribute to the exhaust structure by supporting Kelvin-Helmholtz instabilities at the outflow boundary (Sasunov et al. 2012; Vörös et al. 2021).

Here we present *in-situ* observations of a magnetic cloud like-ICME at Earth's orbit on 20 April 2020. The ICME originated from a quiet-Sun region as a stealth CME **and** drove a shock and sheath region having a relatively strong magnetic field still at the Earth's orbit (O'Kane et al. 2021). The structure and radial evolution of the ICME in the inner heliosphere have been previously analyzed by multiple authors **(Davies et al. 2021; Freiherr von Forstner et al. 2021; Kilpua et al. 2021; Farrugia et al. 2023)**. The event **displayed** a complex structure, where a mixing layer and an ICME front region are identified between the sheath and magnetic cloud proper. We perform a multi-point analysis of the boundary separating these layers **and** considering the mixing layer (ICME front region) ultimately as a part of the sheath region (ejecta). The boundary initially marked by an abrupt increase of magnetic field intensity becomes bifurcated and more gradual and fine structured over small radial distances. The observed dynamics at the ICME sheath–ejecta boundary highlight the importance of continuous multi-point high time-resolution magnetic and plasma measurements in the solar wind at the Earth's orbit: The boundary can exhibit strong spatial variation and while many observations favor an occurrence of magnetic reconnection, the time-resolution of analysed plasma measurements is not sufficient to resolve the boundary structure unambiguously.

The most drastic space weather storms in the Earth's magnetosphere are driven by ICMEs. At global scales, the dynamics at the boundary regulates this interaction. We focus on its local nature, and find a significant lack of coherence from point to point at larger scales within the ICME mixing layer**. This incoherence** complicates space weather predictions.

2. OBSERVATIONS

2.1. *The ICME and its front boundary on 20 April 2020 at 1 AU*

Figure 1 shows the ICME on 20-21 April 2020 observed by the Wind spacecraft (Lepping et al. 1995; Ogilvie et al. 1995) at 1 AU. The figure displays 1 min measurements of the magnetic field (**B**), proton velocity (**V**), proton density (n), temperature (T), and plasma-β in the Geocentric Solar Ecliptic (GSE) -coordinates. We show $-V_X$ in panel d to facilitate comparison. The marked boundaries defined by different authors (Davies et al. 2021; Kilpua et al. 2021) show an ICME which in addition to a coherent magnetic cloud consisted of preceding and trailing non-magnetic-cloud-like ejecta signatures. We name these as magnetic cloud front region (MCFR) and rear region (MCRR) following the terminology of Kilpua et al. (2013). The ICME was furthermore preceded by a shock and sheath region. We identify a mixing layer (ML) between the sheath proper and MCFR defined as the region in front of an ejecta with abrupt latitudinal and azimuthal field rotations and properties of magnetic reconnection including decreased magnetic field magnitude, relatively high proton density, temperature and plasma-β (Wei et al. 2003). Such layers contain a mix of interacted sheath and ejecta plasmas resulting from magnetic reconnection between the regions (Wei et al. 2003; Vörös et al. 2021). The mixing layer is also distinguished by the larger speed and V_Z compared to its surroundings. In this study, we focus on the front boundary of the ICME shown by the vertical solid magenta line in the figure. The boundary separates the confined ejecta from the ambient medium. This boundary can be also regarded as the ICME sheath-ejecta boundary or ICME leading edge, the mixing layer being considered ultimately a part of the sheath region.

We examine measurements from the Wind, Advanced Composition Explorer (ACE) (Stone et al. 1998), Deep Space Climate Observatory (DSCOVR) (Burt & Smith 2012), Time History of Events and Macroscale Interactions during Substorms C (Themis C) (Angelopoulos 2008) spacecraft, and from the Cluster (Escoubet et al. 1997) and Magnetospheric Multiscale (MMS) (Burch et al. 2016) missions, which were closer to the Earth but still in the solar wind. Figure 2a-b show the spacecraft positions during the ICME front boundary passage in the GSE XY- and YZ-planes in Earth radii ($\mathrm{R_E}$). The solar wind monitors at the Lagrange L1 point were at $200-250\,\mathrm{R_E}$ from the Earth**,** and within $110\,\mathrm{R_E}$ ($25\,\mathrm{R_E}$) from each other along GSE Y-axis (Z-axis). Themis C was at $50\,\mathrm{R_E}$ from the Earth, and Cluster and MMS at $10-11\,\mathrm{R_E}$. The spacecraft separations correspond to 0.3-70 min time scales.

Figure 2c-f show magnetic field magnitude and GSE-components during the ICME front boundary passage at different locations with time-resolutions of 1 s for ACE, 1 s for DSCOVR, 0.092 s for Wind, 4.1 s for Themis C, 0.062 s for MMS 1, and 0.045 s for Cluster 4. These magnetic field time-resolutions are used throughout in this study unless mentioned otherwise. In the figure, the solar wind monitor and Themis C measurements are time-shifted relative to MMS and Cluster using the solar wind velocity measurements and spacecraft separation along the X-axis. The ICME front boundary is marked by the significant increase of the field magnitude up to $14-15$ nT, and simultaneous abrupt rotation of the field components. The similar field enhancement with the other spacecraft at Cluster 4 and MMS 1 indicates these magnetospheric missions were in the solar wind during the event. Figure 2c shows short distinct field depressions adjacent to the boundary at DSCOVR and Wind. The magnetic field was relatively weaker also at MMS 1 and Cluster 4 before the field enhancement, but at ACE and Themis C the feature was less evident. The transition to the high field values happened more abruptly at the solar wind monitors (ACE, DSCVOR, Wind) and at Themis C, and was more gradual at Cluster 4 and especially at MMS 1.

Figure 2d shows similar B_X between ACE and Cluster 4, and **between** Themis C and MMS 1 across the boundary. Especially distinct rotations of B_Y occurred at ACE, Themis C**,** Cluster 4, and MMS 1. These rotations are highlighted by pale magenta for B_Y at Themis C in panel e**:** A large-scale rotation was followed by an oppositely directed rotation at all four spacecraft. Both rotations imply the presence of current sheets as predicted by Amprére's law. The large-scale B_Y-rotation occurred in two steps at the MMS location showing the profile of a bifurcated current sheet. Another rotation of B_Y occurred shortly after **the opposite rotation** at ACE and Cluster 4. Furthermore, the field magnitude change occurred predominantly in B_Z at all spacecraft. ACE and Themis C observed a B_Z profile which resembles a rotation happening in two steps but which can also be associated with the trend measured by MMS 1. Detecting these features at DSCOVR or Wind is more ambiguous. For further analysis, we transfer to the local boundary normal coordinates and examine measurements from each spacecraft separately.

2.2. *Local Boundary Normal Coordinates*

We use local boundary normal coordinates, where the local normal is defined by the cross product $\mathbf{N} = \mathbf{B_1} \times \mathbf{B_2}/|\mathbf{B_1} \cdot \mathbf{B_2}|$, where $\mathbf{B_1}$ and $\mathbf{B_2}$ are the average magnetic field directions on either side of a current sheet. In our analysis, the studied interval is bounded by intervals marked by pale blue shading in **Figures 3-5, 7, and 9**. These intervals give the downstream and upstream values used to determine the normal direction. The maximum variance direction given by the minimum variance analysis of the field ($\mathbf{L_{mva}}$) across the current sheet (Sonnerup & Scheible 1998) is used to determine the unit vectors orthogonal to the normal:

$\mathbf{M} = \mathbf{N}\times\mathbf{L_{mva}}/|\mathbf{N}\cdot\mathbf{L_{mva}}|$, and $\mathbf{L} = \mathbf{N}\times\mathbf{M}$. This boundary normal coordinate LMN-system is often used instead of the MVA, being considered as a more robust method (Knetter et al. 2004; Vasquez et al. 2007; Eriksson et al. 2022). It is known either as the cross-product method (Knetter et al. 2004) or the hybrid-MVA (Gosling & Phan 2013; Eastwood et al. 2021). Across a reconnection exhaust, **L** (**N**) indicates the outflow (inflow) direction, with B_L often showing the profile of a bifurcated current sheet with a two-step rotation. **M** gives the out-of-plane direction and B_M the reconnection guide-magnetic field.

2.3. *Walén relation*

We compute the Walén relation using plasma measurements, which are available for the event from Wind, Themis C and Cluster 4 at 3, 4.1 and 4.2 s time-resolutions, respectively, but absent or available only at too sparse time-resolutions from the ACE, DSCOVR, MMS and other Cluster spacecraft. The relation is given as (Walén 1944; Sonnerup et al. 1981; Paschmann et al. 1986)

$$V_{WL} = V_{L,ref} \pm \sqrt{\frac{\rho_{ref}}{\mu_0}}\left(\frac{B_L}{\rho} - \frac{B_{L,ref}}{\rho_{ref}}\right), \tag{1}$$

where ρ is the mass density, μ_0 the vacuum permeability and the subscript "ref" refers to the reference value given by the upstream and downstream of the studied interval. It tests the tangential momentum balance across an interval and is used to examine plasma flows in potential magnetic reconnection exhausts. The test is often applied to the flows in the L-direction, which points to the direction of the reconnection outflow (e.g. Eriksson et al. 2009, 2014, 2022; Mistry et al. 2015a, 2016; Phan et al. 2020), and without the expectation of a larger $|V|$ within a reconnection exhaust relative to the surroundings (Phan et al. 1996). It is performed separately from both sides of the studied interval. The predictions conducted from different sides use opposite signs in Equation (1), since correlated and anti-correlated V_L and B_L are expected across the structure boundaries. The Walén prediction has a tendency to produce larger exhaust flow velocities than observed in space and numerical simulations (e.g., Phan et al. 1996; Le et al. 2014).

2.4. *Single-Spacecraft Analysis*

2.4.1. *DSCOVR and ACE*

Figure 3a and 3c (3b and 3d) show magnetic field in local LMN-coordinates at DSCOVR (ACE), with the blue shading indicating the intervals used to determine the normal direction. The red horizontal bar marks the interval shown in Figure 3e (3f). At DSCOVR, all the components experienced rapid changes across the boundary defined by the abrupt field intensity enhancement, with B_M following the field magnitude profile and having a change in two steps. The boundary**, which was preceded by** a short local dip in the magnitude**, did not show** signatures of bifurcated B_L. **However**, after the most abrupt field increase, B_L had a gradual bipolar rotation which was followed by an opposite rotation associated with a minor field strength increase. Figure 3c shows that further in the ejecta, notable field fluctuations occurred.

ACE observed a sudden change of B_L with no bifurcation, which was followed by a gradual opposite rotation and a second additional sharp rotation. These B_L-rotations together mark an interval which shows a bipolar variation of B_M with respect the black dashed line in Figure 3d. The bifurcation of the B_Z-component at ACE shown in Figure 2f is no longer present in the LMN-coordinates.

2.4.2. *Wind*

Figure 4a-b show the Wind magnetic field measurements and Figure 4c-f 3 s plasma measurements for the ICME front boundary. Figure 4d-e give the proton and electron velocities, with panel d showing the Walén prediction for V_L performed separately from the each side of the boundary (black and gray dotted curves). Figure 4f shows the diamagnetic current density (J_D)

$$J_D = (T_i + T_e)k_B\frac{\mathbf{B}\times\nabla n}{B^2}, \tag{2}$$

where T_i and T_e are the ion and electron temperatures, k_B is the Boltzmann constant, and n is the plasma number density. We use the solar wind V_N to estimate the density gradient in single spacecraft measurements.

The sharp increase of $|B|$ was preceded by a region of decreased field strength caused by the weakening B_L-component. The decrease was simultaneous with local enhancements of proton and electron densities shown in panel c. The proton speed did not vary significantly across the boundary but had a local minimum just before the field decrease on the sheath side, increased within the decrease and reached a local maximum at the boundary. This maximum was associated with an enhancement of proton V_L, which deviated from the surrounding values. The observed proton V_L is in a good agreement with the Walén prediction both showing a double-peaked V_L to the negative L-direction. The prediction carried from the sheath side (black dotted curve) has some magnitude and timing differences before the ICME front boundary, where the significant V_L enhancement occurred. The predictions performed from the different sides cross each other at the boundary and predict this jet with an over-estimation. Significant electron V_L peaks and enhanced diamagnetic currents occurred during the field strength drop. The latter electron V_L peak had minor timing difference with the proton V_L peak.

In addition, Figure 4b shows a two-step rotation of B_L across the sharp $|B|$ jump **at the boundary**, which is coincident with the observed proton V_L jet predicted by the Walén relation. $|V|$ was also slightly larger within the bifurcation compared to the immediate surroundings. The stronger electron V_L jet is aligned with the first sharp increase of $|B|$ at 07:54:30. The following major field increase is aligned with a B_L change and the proton V_L peak.

2.4.3. *Themis C*

Figure 5 shows the boundary crossing at Themis C, which was located about 150-200 R_E earthward from the three solar wind monitors near L1. The panels follow the organization of Figure 4, panel g showing the parallel (solid) and perpendicular (dotted) proton and electrons temperatures relative to the magnetic field.

In contrast to DSCOVR and Wind, Themis C did not observe a dip in the magnetic field magnitude adjacent to the boundary. Across the boundary, B_L shows a strong variation associated with a bipolar profile of B_M with respect to the level shown by the dotted black **line** in the figure. A bipolar B_M was not observed by DSCOVR or Wind and by ACE only when examining the field measurements further in the ejecta. The field components in the local LMN-coordinates at Themis C did not record a bifurcation nor the distinct opposite rotation of the major rotation component seen in Figure 2.

Local density minima aligned with the abrupt field increases in Figure 5 demarcated a denser plasma region within the boundary and marks a deviation from the general density drop profile between the sheath **and** ejecta in panel c. Although the proton speed did not show significant changes across the boundary, proton V_L was larger having a rapid increase after the sheath and a gradual decrease towards the ejecta side. The Walén prediction overestimate the observed V_L, but the temporal evolution is similar with the predictions from the different sides, which again cross at the V_L maximum. The ejecta side prediction (gray dotted curve in Figure 5e) shows a sharp dip in the velocity which was captured by the electron measurements. The electron V_L shows bipolar two-sided jets, which were reflected also in the diagmagnetic current density measurements. The temperature anisotropies of both protons and electrons were well below one ($T_\perp/T_{||} < 1$) within the boundary due to the general enhancement of the parallel components and several distinct proton $T_{||}$ peaks seen in Figure 5g.

2.5. *Multi-Spacecraft Analysis*

The single-spacecraft observations of the ICME sheath-ejecta boundary on 20 April 2020 were followed by Cluster and MMS observations. Figure 6 shows the Cluster and MMS constellations during the event. The MMS formation was close to a perfect tetrahedron indicated by the close-to-one Q-factor of 0.96, which indicates a robust current density estimation performed with the curlometer technique (Robert et al. 1998; Dunlop et al. 2002). The MMS spacecraft were within 0.044 - 0.056 R_E distance from each other. Cluster had instead an elongated formation, the inter-spacecraft separations varying between 0.4 and 1.6 R_E. The curlometer technique is not reliable for **a such** formation as demonstrated by the low Q-factor of 0.05.

2.5.1. *Cluster*

Figure 7 shows the magnetic field measurements from the Cluster 1 - 4 spacecraft in the local LMN-coordinates. All Cluster spacecraft observed a minor field magnitude decrease before the boundary, resembling the observations from ACE. The field increase across the boundary was however more gradual at Cluster in comparison to the earlier measurements **(DSCOVR, ACE, Wind, Themis C)**. The boundary consisted of three distinct sharp field jumps shown in Figure 7a. Panels a-b show an alignment between these jumps and changes of B_L, the changes being highlighted by pale blue in panel c. Localised features occurred in the measurements, Cluster 3 (C3) observing a distinct rotation of B_N within the boundary. At the ejecta edge of the boundary, a local dip in the field magnitude was **only** observed by C4. The red horizontal bar in Figure 7b marks an interval, which is shown in a zoomed-in view in Figure 7c for C1 and C2 and for C3 and C4 in Figure 7d. B_L experienced a multi-step variation across the boundary with a following opposite rotation. The steps are highlighted by pale blue and magenta in panel c, respectively. All the steps were observed by all the Cluster spacecraft expect C2, which saw a more gradual variation of B_L without the plateau between the second and third rotations (the second and third pale blue highlightings from the left in panel c). B_M experienced a bipolar structure through the boundary relative to the dotted magenta line shown in Figure 7e. The opposite rotation of B_L highlighted by pale magenta in panel c coincided with a B_M-rotation.

Figure 8 shows $|B|$ and B_L together with the plasma measurements from C4, C1-3 having no recorded plasma measurements during the event. The organization of the panels follows Figure 4, with panel e giving the proton temperature parallel and perpendicular to the magnetic field. In this scale, the dips in $|B|$ across the boundary appear more clearly. Furthermore, density had a two-step drop within the transition from sheath to ejecta, the major B_L-variation coinciding with the most significant drop in density. The major drop was followed by two local density enhancements before ejecta values. The latter enhancement occurred simultaneously with the opposite B_L-rotation. Both $|V|$ and V_L were enhanced within the boundary and show a double-peaked structure in Figure 8d. The first jet is aligned with the major B_L change. The enhanced $|V|$ occurred simultaneously with a local B_M decrease, the bipolar pattern occurring across a wider interval (see Figure 7). Similar to Wind and Themis C observations, the Walén relation follows the observations (over-) predicting the two-sided **jet**, the first jet shown by the crossing of the predictions from sheath and ejecta sides. Within the boundary, parallel proton temperature was smaller and a temperature anisotropy $T_\perp/T_{||} > 1$ briefly occurred.

2.5.2. *MMS*

Figure 9 shows the ICME boundary layer crossing on 20 April 2020 at MMS. Magnetic field measurements shown in panels a-b did not differ from each other between the individual spacecraft and the values shown in Figure 9 represent the observations of MMS 1-4. During the $|B|$-increase, the L-component had a large-scale bifurcated rotation occurring in two steps. The bifurcated current sheet was followed by an opposite rotation of B_L and **a rotation of** B_M. In panel b, B_M shows a bipolar profile across the B_L-rotations, the profile being displayed relative to the reference level marked by the dotted black line in Figure 9b. The variation of B_M is also aligned with the first jump of the relatively gradual increase of $|B|$ through the boundary.

Figure 9c shows the total current density ($|J|$) estimated using the curlometer technique. Together with its 2-second moving average, $|J|$ in panel c reveals enhanced currents during the field increase with high filamentation and major current peaks in the L- and M-directions. The averages highlight a structure which is aligned with the field rotations. Additionally, MMS observed a wide double-peaked distribution associated with the second step of the bifurcated current sheet in the middle of the boundary layer.

Plasma dynamics can cause non-linear gradients of the magnetic field, which can lead to non-zero magnetic field divergence and inaccurately resolved current vectors when applying the curlometer technique to the four-point constellation measurements. These inaccuracies are negligible for $|\nabla\cdot\mathbf{B}|/|\nabla\times\mathbf{B}| \ll 1$, with the value of 0.5 being used as a threshold for reliability (Dunlop et al. 2002; Haaland et al. 2004). The ratio is given in Figure 9e, with the dashed orange line marking unity. The gray (teal) bars at the bottom of Figures 2c-d indicate the times during which the ratio was below 0.5 (1), with panel d showing the times for the averaged curve. Despite the spikes in panel e, which indicate uncertainties in the current estimation, the method is reliable for most of the studied interval.

Plasma measurements were only available for high-energy ions during the event at MMS. The measurements were measured with a 10 s time-resolution and did not capture distinct features across the boundary (not shown).

Table 1 supplements this section showing the GSE-components of the local LMN-coordinates used in this study and also providing the magnetic shear angles and $|B_M/B_L|$ ratios across the ICME front boundary.

2.6. *Spatial Variation and Radial Evolution of the Mixing Layer*

Finally, we compare the mixing layer identified in Figure 1 at different spacecraft including the observations of $|B|$ from Solar Orbiter (Müller et al. 2013). Figure 10a-c show the magnetic field magnitude and the field azimuthal and GSE Z components across a wider interval around the ICME sheath-ejecta boundary at 1 AU at 1 min time-resolutions. The data are shown with arbitrary time-shifts from different spacecraft. The figure highlights the mixing layer at different locations based on the rapid and substantial ϕ_B-rotations, which occurred primarily within the interval of decreased $|B|$. While all spacecraft observed highly fluctuating ϕ_B, decreased magnetic field intensity is less prevalent at DSCOVR. Furthermore, B_Z experienced significant spatial variation between the spacecraft. The start of substantial ϕ_B-rotations is aligned with an abrupt rotation of B_Z from northward to southward **at all spacecraft**. At L1, ACE and especially DSCOVR observed a field that maintained a strong negative B_Z across the mixing layer, whereas Wind observed only brief intervals of negative B_Z. ACE data shows a significant dip of $|B|$ which is associated with a near-zero B_Z. Themis C, MMS 1 and Cluster 4 observed a weaker southward field than ACE and DSCOVR, the field experiencing notable fluctuations and temporarily turning northward.

The $|B|$ measurements from ACE and Wind are furthermore compared to those from Solar Orbiter, which observed the ICME on 19 April 2020 at the distance of 0.8 AU from the Sun. Figure 10d shows the start of ICME ejecta with magenta vertical lines. Closer to the Sun, the ejecta followed plasma that showed a multi-step $|B|$ enhancement from the solar wind to the ejecta. The

ICME front was preceded by a mini flux rope (Kilpua et al. 2021), which caused the second field enhancement shown in the figure. The mini-flux rope extended up to the ICME front, where a shorter and less prevalent dip of the magnetic field occurred than at the solar wind monitors.

3. DISCUSSION

We report multi-point observations of an ICME mixing layer and ejecta front boundary in April 2020, examining measurements from solar wind monitors at L1, magnetospheric missions in the solar wind, and from Solar Orbiter at the distance of 0.8 AU from the Sun. The spacecraft measurements revealed differences at the boundary, which imply evolution over radial distances of $237\,\mathrm{R_E}$ and spatial variation over transverse distances of $114\,\mathrm{R_E}$**. In addition, the Cluster mission distinguished localized structures while having** $0.4-1.6\,\mathrm{R_E}$ inter-spacecraft separations. **Different spacecraft generally** observed an abrupt change of the B_L-component**, a following** opposite B_L-rotation**, and** a bipolar B_M **at the boundary. Interestingly,** the mixing layer **displayed substantial differences** in the geoefficient B_Z-component. We interpret our results below and list features in data which favors magnetic reconnection at the boundary.

3.1. Ambiguous Reconnection Signatures at Wind

At Wind, the $|B|$ decrease occurred with simultaneous increases in densities. A similar dip in the field magnitude occurred at DSCOVR but not at ACE. The Walén prediction and the observations show no clear velocity enhancement profile across the $|B|$ decrease, which may show a trace of a reconnection exhaust where the jet has already experienced dissipation. The weakened field interval however hosted a one-sided proton V_L jet and double-peaked electron velocities.

The relatively low time-resolution 3 s plasma measurements at Wind leave our interpretation ambiguous. The gradual changes in plasma variables complicate the identification of slow-mode waves, which can also be undetectable due to an oblique spacecraft path across a reconnection exhaust (Walia et al. 2022). Consequently, no separation between a reverse wave and the ICME ejecta front boundary can be made. The outflow plasma can also interact with the ambient medium at the exhaust boundaries (Sasunov et al. 2012; Lapenta et al. 2017; Vörös et al. 2021). The most significant proton and electron V_L jets indicate reconnection in the proximity of the boundary, but cannot be unambiguously related to dynamics within the field depression or at the very boundary marked by the abrupt field increase. They occurred right at the boundary, where the sharp multi-step increase of $|B|$, a bifurcation of B_L, and a weak local maximum of $|V|$ **were** observed. We however repeat that a larger $|V|$ relative to the surroundings is not a strict requirement for magnetic reconnection identification (e.g., Phan et al. 1996).

3.2. Outflow of Asymmetric Reconnection with Hall Fields at Themis C

At Themis C,

a large rotation of B_L together with the bipolar B_M, local density enhancement and proton V_L increase overpredicted but followed by the Walén relation suggest that Themis C observed magnetic reconnection exhaust across the ICME front boundary. We note that the prediction showed an opposite V_L jet, which was not observed. The proton V_L instead peaked at the sheath side of the boundary decreasing gradually towards the ejecta. Such a profile can be observed in a single exhaust crossing of asymmetric reconnection, where the inflow conditions from one side dominates the dynamics. As a consequence, a weaker or absent jet occurs at the other edge of the exhaust (see e.g., Section 2 by Owen et al. 2021).

The bipolar B_M resembled the Hall fields. The Hall fields are generated by the Hall currents, which result from the different decoupling scales of plasma protons and electrons and which flow toward and away from the diffusion region along the outflow direction (the L-direction) (Eastwood et al. 2010; Denton et al. 2016; Peng et al. 2017; Dai 2018). These currents create a bipolar B_M profile in spacecraft observations in a single-exhaust crossing (Mistry et al. 2016). The profile is distorted in the presence of a guide field (non-zero inflow B_M), becoming asymmetric across the normal axis (Eastwood et al. 2010).

3.3. Density Cavities at Themis C: Guide Field Reconnection and Magnetic Islands

Guide field reconnection is observed to introduce density cavities to an exhaust edge. Such cavities host parallel ion heating and parallel electron cooling in addition to the parallel heating of the plasma happening in the main exhaust (Eastwood et al. 2018). Consistent with these observations, the boundary observed by Themis C hosted $T_{||}$-heated plasma**,** and density dips at the edges which coincided with local parallel heating of protons. Signatures of electron cooling were however absent. Magnetic reconnection accelerates electrons which show a jet close to the B_M reversal in guide field reconnection (Wilder et al. 2017). The cavities, on the other hand, are associated with electron flows toward the X-line (Eastwood et al. 2018). The observed electron jet to the positive L-direction at Themis C may correspond the electron outflow from the X-line, with the jet to the negative direction at the ejecta side showing a cavity related flow toward the X-line. We however note that there is a timing difference between the electron outflow and B_M reversal. Regular higher time-resolution plasma measurements in the solar wind would enable a more detailed analysis. We also observe density decreases at both edges. While local density minima can occur right outside of reconnection exhaust edges (Phan et al. 2016) or within the exhaust near the edges (Eastwood et al. 2018), the cavities of guide field reconnection occur only at one edge (Eastwood et al. 2018; Che et al. 2021).

The density minima may also result from the formation of magnetic islands due to multiple reconnection X-lines (Eriksson et al. 2014, 2015), which produces two-sided (bipolar) electron flows and a so-called overshoot of the B_L-component, which is followed by a bifurcation and an opposite rotation. Themis C measured such bidirectional two-sided electron flows and an overshoot on the sheath side right before the major B_L-rotation. Similar overshoots were also observed by ACE, Cluster and MMS. However, while the magnetic field GSE-components showed a multi-step rotation, a bifurcated B_L and a tripolar B_M were not observed at Themis C. We note that the field fine structure may have been missed by Themis C due to its relatively low 4.1 s time-resolution measurements. A clear bifurcation typically develops only at large distances (∼1000 ion skin depths d_i) from the reconnection site (Mistry et al. 2015b) but can also appear closer to the X-line ($\sim 130\,d_i$) in long-lasting reconnection (Innocenti et al. 2015).

3.4. Localized Structures and Two-Sided Jet at Cluster

The boundary fine structure was evident in Cluster measurements, with magnetic field structures being solely observed by individual spacecraft, which were within 1.6 $\mathrm{R_E}$ from each other. For example, Cluster 4 observed a local dip in the magnetic field which was associated with density and velocity enhancements and not observed by the other Cluster spacecraft. Cluster 3 on the other hand observed a distinct B_N-rotation. Compared to the earlier measurements, Cluster observed a multi-step gradual increase of field magnitude, which hosted minor field depressions. The field jumps coincided with changes in the B_L-component**.**

Cluster 4 observed a distinct double-peaked velocity enhancements across the boundary. Such velocity signatures are called bifurcated outflow jets (Liu et al. 2021) or two-sided jets (Enžl et al. 2017). We use the term "two-sided jets" in this study to avoid confusion with a bifurcated current sheet, which is manifested by a two-step field rotation. Two-sided jets develop in a multiple or patchy reconnection exhaust (Enžl et al. 2017) when the reconnection outflow interacts with the preceding slower exhaust plasma (Liu et al. 2021). The inhomogeneous plasma conditions drive multiple reconnection sites or patchy reconnection regulating the outflow properties, such as jet speeds (Enžl et al. 2017). The central region of the faster outflow overtaking the slower flow is slowed down at the interface with high-speed jets forming at the exhaust boundaries.

Patchy reconnection with a finite length of the X-line can furthermore result in a one-sided jet (Enžl et al. 2017) and explain the jet in the Wind observations. And when including another weak V_L enhancement to the negative L-direction at the sheath side into consideration, two-sided jets can also be identified in the Wind data. Similar to the other jets reported in this study, this enhancement is also over-predicted by the Walén relation.

3.5. Bifurcated B_L and Filamentary Currents at MMS

The boundary fine structure was further revealed by MMS which observed a clear bifurcated current sheet populated by filamented currents. The filamentation can be attributed to plasma dynamics that generates spatio-temporal variations at turbulent reconnection exhausts, where filamentary currents coexist with enhanced field variations (Fu et al. 2017; Huang et al. 2017; Wang et al. 2022). Field variation levels, measured as the mean of $\sum_{i=1}^{N} |\mathbf{B}_{i+1} - \mathbf{B}_i|$, are 0.14 (0.05), 0.09 (0.03), and 0.09 nT (0.03 nT) for B_L, B_M, and B_N within (outside) the potential exhaust region within the boundary, respectively. The difference of successive points is taken to subtract the large-scale field rotations. Reconnection becomes turbulent especially in low-β plasmas (Higashimori & Hoshino 2015).

Significant J_M currents were associated with transverse B_L-rotations at MMS, where the bipolar variation of B_M is in qualitative agreement with previous observations across a reconnection exhaust (Mistry et al. 2016). Similar currents aligned with a bifurcation have been previously observed in the vicinity of an ICME inner boundary (Chian & Muñoz 2011). In a reconnection exhaust, such currents can result from the breaking of the original current sheet or from plasma gradients, which drive field suppressing diamagnetic currents (Owen et al. 2021). Multiple field depressions occur within the crossing in Figure 9, aligned with the field rotations. Also, kinetic instabilities introduce fine structure to reconnection current sheets (e.g., Mistry et al. 2015a, and references therein). Unfortunately, the necessary plasma measurements for a conclusive identification of the current carriers were unavailable for MMS during the event. Wind and Themis C data however show diamagnetic currents at the boundary.

3.6. Summary of Low-Shear Magnetic Reconnection at the ICME Sheath-Ejecta Boundary

The right column of Table 1 summarises our conclusions about magnetic reconnection at different locations. The observed reconnection signatures are not inhibited by the low magnetic shear ($11° - 35°$) present across the ICME front boundary on 20 April 2020. Magnetic reconnection occurs within ICMEs even with extremely low magnetic shears, with values of $4° - 9°$ and $27° - 37°$ being observed (Gosling & Phan 2013; Phan et al. 2020). This is however the first report of (one) two-sided jets **that were** associated with magnetic shear angle $< 40°$ (Enžl et al. 2017).

In addition to reconnection, electron and proton anisotropies ($T_\perp/T_{||} > 1$) as well as the Speiser orbit of energized heavy ions cause bifurcated current sheets (George & Jahn 2020; Jiang & Lu 2021, and references therein). Such anisotropies were however absent in the analyzed measurements with the exception of a short term anisotropy peak observed by Cluster 4. Continuous high time-resolution plasma and heavy-ion measurements in the solar wind would enable investigation of different scenarios in detail. They would, for example, improve the understanding of the opposite B_L-rotation observed at several spacecraft. Such rotations may appear in multi-layered outflows during asymmetric reconnetion (Owen et al. 2021). In addition, magnetic reconnection is regulated by the ionospheric cold ions at the Earth's magnetopause (e.g., André et al. 2016). ICMEs often show elevated amounts of high charge state heavy ions with solar origin, whose impact on reconnection remains still unrecorded in in-situ measurements. We also note the expansion of the ejecta also contributes to the dynamics at the ICME front boundary by compressing structures emanating at the boundary.

3.7. Mixing Layer Introduces Uncertainty to Space Weather Predictions

Finally, the reconnection at an ICME front boundary results in a mixing layer, which based on our results evolves over both large (0.2 **AU**) and small ($237\,R_E$) radial distances. **The evolution over larger distances is consistent with the findings by** Farrugia et al. (2023)**, who analyzed the same ICME event concluding that the ejecta front eroded between Solar Orbiter to Wind.**

At 1 AU, we observed major differences in the mixing layer between ACE - MMS, and a lack of coherency in B_Z occurred even between Themis C and Cluster ($42\,R_E$ radial and $21\,R_E$ transverse separations). Substantial B_Z variations also occurred in the mixing layer in the transverse direction between the L1 solar wind monitors, which were within $114\,R_E$ from each other in the GSE YZ-plane. Wind observed only temporary southward fields during the mixing layer whereas DSCOVR measured a strong steady negative B_Z.

Space weather predictions are dependent on observations at L1. OMNI data, which are often used as the reference for the upstream conditions in magnetospheric studies, for example was derived from the Wind measurements during the event. Our results imply that care ought to be taken when making predictions during the passage of ICMEs and their sheath regions, which are key drivers of magnetopsheric activity (Huttunen et al. 2002; Huttunen & Koskinen 2004). Their space weather impact may vary due to local dynamics in proximity to the ICME sheath-ejecta boundary. The uncertainties in upstream solar wind conditions have been noted recently by several authors (e.g., Borovsky 2018; Walsh et al. 2019; Di Matteo & Sivadas 2022; Sivadas & Sibeck 2022).

4. CONCLUSIONS

In summary, we have presented multi-spacecraft *in-situ* observations of magnetic reconnection at an ICME sheath–ejecta boundary on April 2020. We analyzed multi-point measurements and identified magnetic reconnection at various locations at the boundary, which hosted **a** two-sided **jet associated with an** unprecedentedly low magnetic shear **angle**. Our results imply several (patchy) reconnection sites along the ICME front boundary (see Enžl et al. 2017; Liu et al. 2021) augmenting earlier work about ICME erosion (Ruffenach et al. 2012). The dynamics at the ICME sheath–boundary exhibited fine structure captured by the Cluster and MMS observations. Individual Cluster spacecraft observed localised structures across the inter-spacecraft separations of 0.4 - $1.6\,R_E$, whereas highly filamented currents were measured by MMS. The measurements were however not sufficient for further specification of the structures or the currents at the boundary.

At larger scales, we identified a mixing layer in front of the ejecta, which experienced substantial southward field variations and a lack of coherency **at 1 AU**.

Magnetic reconnection outflows at an ICME sheath–ejecta **interface** are shown to interact with the ambient plasma at magnetohydrodynamic and kinetic scales at the outflow boundaries, where various dynamic processes occur (e.g., Lapenta et al. 2017; Hesse et al. 2018; Vörös et al. 2021) including Kelvin-Helmholtz instability (Sasunov et al. 2012; Vörös et al. 2021). It is important to understand the interplay between the small- and large-scale dynamics of the mixing layer and the front boundary of an expanding ICME ejecta, because at Earth the dynamics introduce uncertainties to space weather predictions.

Solar Orbiter and Parker Solar Probe (Fox et al. 2016) enable studying the ICME sheath-ejecta boundary and the mixing layer at various sub-1 AU-distances from the Sun. Analyzing their high time-resolution magnetic field, proton and electron measurements can help to specify the dynamics at the ICME ejecta front boundary as well as the mixing layer formation (e.g., Owen et al. 2021)**. Future research about the mixing layer including resolving the distances of its initiation will result in a better understanding of the ICME evolution.**

Finally, our study augments the multi-point research of ICMEs at the Earth's orbit (Lugaz et al. 2018, 2022; Ala-Lahti et al. 2020, 2021; Vörös et al. 2021). Together with previous work, it highlights the need for continuous (sub)second-resolution plasma and field measurements at multiple locations in the solar wind which can address the spatio-temporal structure of ICMEs. These results should direct the future spacecraft mission design which aims at discovering the detailed structure and evolution of ICMEs (e.g., Allen et al. 2022; Akhavan-Tafti et al. 2023; Nykyri et al. 2023).

The Space Weather Investigation Frontier (SWIFT; Akhavan-Tafti et al. 2023) is a multi-spacecraft mission concept dedicated to addressing these questions including the ICME three-dimensional structure and dynamics. The mission aims to provide continuous measurements along the Sun-Earth line beyond the Lagrange L1 point (sub-L1), doubling the current forecasting lead-times. In Table 2, we list desired probe separations and time-resolutions for the SWIFT mission according to the discoveries made in this study. The spatial coherence of ICME sub-structures requires further study at various transverse probe separations and in Table 2, we double the maximum separation analyzed in this study ($\sim 110\,\mathrm{R_E} \rightarrow 220\,\mathrm{R_E}$). A four-probe mission with (sub)second-resolution plasma and field measurements and varying inter-spacecraft separations is required for a comprehensive examination that covers the dynamics at small and large scales. However, as demonstrated by the analyzed Themis C and Cluster 4 measurements, sub-L1 measurements at ~ 4 s time-resolution together with observations from current missions at L1 can also improve our understanding of ICME three-dimensional substructures and dynamics.

Data reported here were first identified by the authors while performing preparatory work for the Space Weather Investigation Frontier (SWIFT; NASA grant 80NSSC23K0674), the data being obtained from the MMS Science Data Center (https://lasp.colorado.edu/mms/sdc/public/), Cluster Science Archive (https://csa.esac.esa.int/csa-web/), and the CDAWeb Archive (https://cdaweb.gsfc.nasa.gov). MA-L acknowledges the Emil Aaltonen Foundation for financial support. TP and MA-L acknowledge support from NSF grant 2033563. SG and JR acknowledge support by the Academy of Finland (INERTUM, grants 338486 and 346612). MAT was supported by NASA contract NNN06AA01C, and grants 80NSSC20K1847, 80NSSC20K1014, 80NSSC21K1662, and 80NSSC23K0674. EK acknowledges the ERC under the European Union's Horizon 2020 Research and Innovation Programme Project SolMAG 724391. EK and SG acknowledge the Finnish Centre of Excellence in Research of Sustainable Space (Academy of Finland grant numbers 312390, 336807). **We wish to thank the anonymous reviewer for their careful evaluation of this work.**

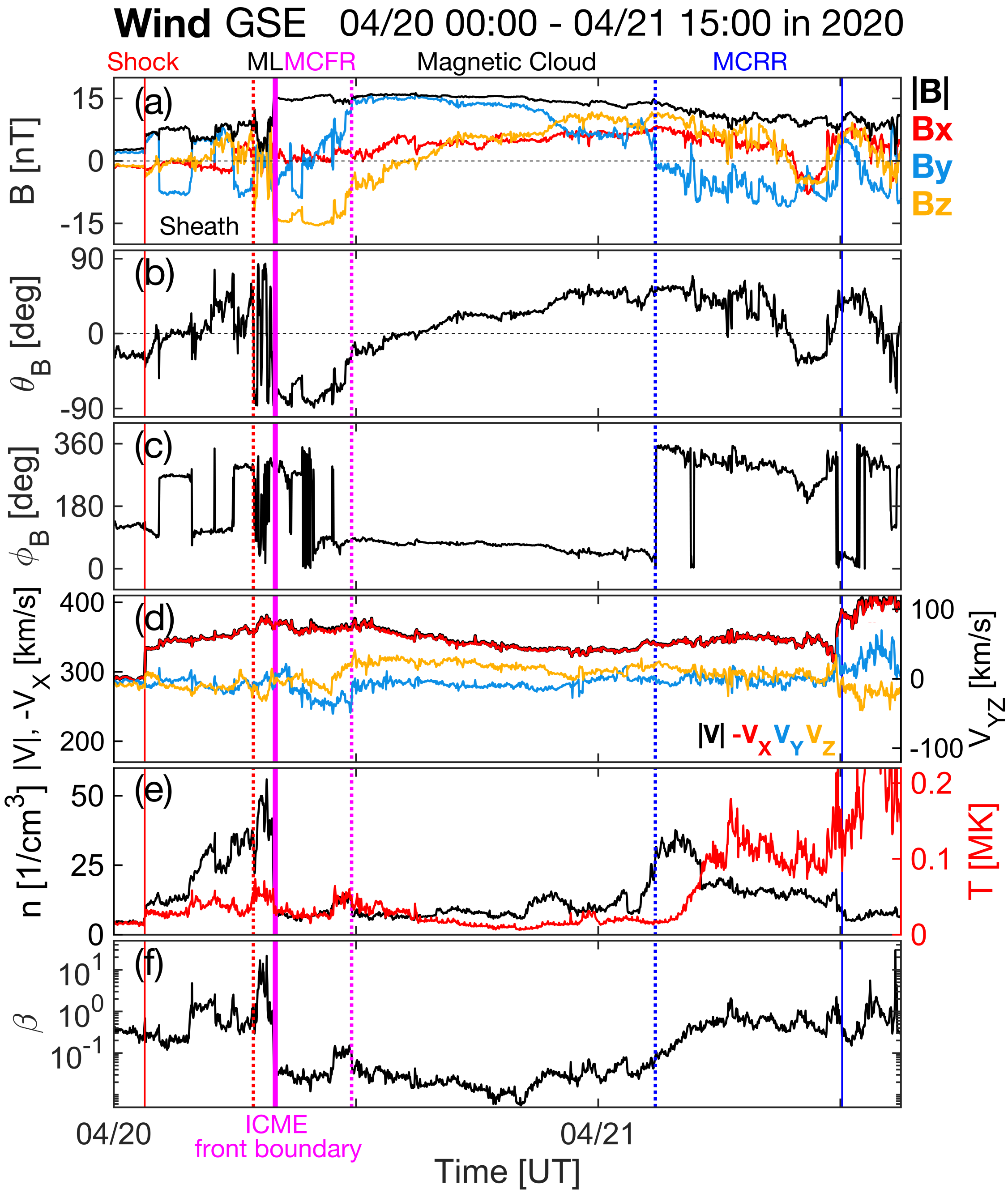

Figure 1. ICME observed by Wind on 20-21 April 2020 at 1 AU. Panels show **(a)** magnetic field (**B**) magnitude and GSE-components, **(b)** magnetic field latitudinal (θ_B), and **(c)** azimuthal (ϕ_B) angular components with respect to the ecliptic plane, **(d)** proton velocity (**V**), **(e)** density (n, black), and temperature (T, red), and **(f)** proton plasma-β. The vertical lines indicate the shock (solid red), the beginning of the mixing layer (dotted red) front boundary of the ICME (solid magenta), magnetic cloud (dotted magenta and blue), and the rear boundary of the ICME (solid blue). In panel d, $-V_X$ is shown to facilitate comparison. Abbreviations: ML - mixing layer MCFR - magnetic cloud front region, MCRR - magnetic cloud rear region.

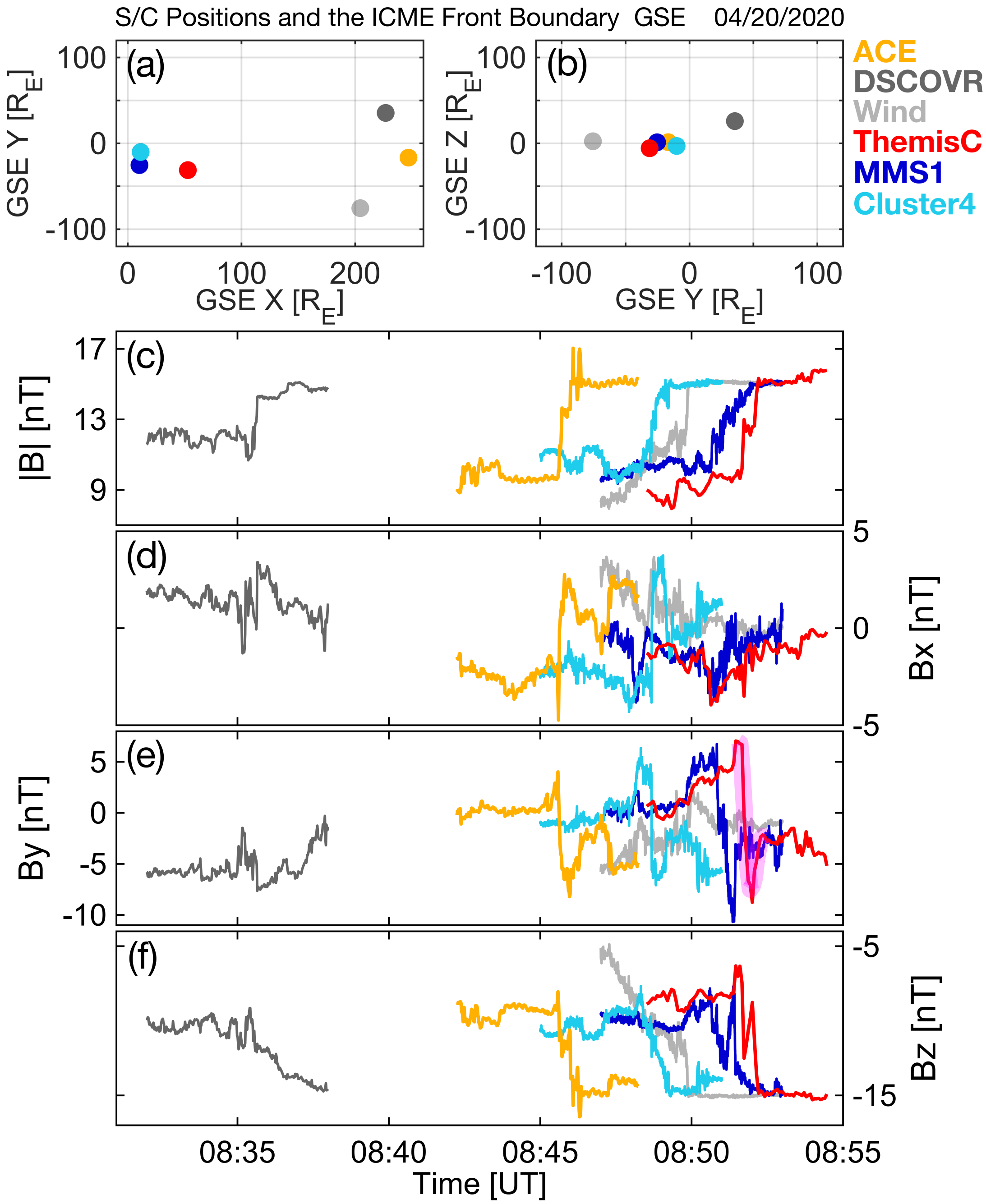

Figure 2. The spacecraft positions and the magnetic field measurements during the ICME front boundary passage on 20 April 2020. Panels show the spacecraft positions in **(a)** the GSE XY-plane, **(b)** YZ-plane in Earth radii (R_E), and the magnetic field **(c)** magnitude, **(d)** GSE X-component, **(e)** Y-component, and **(f)** Z-component. The solar wind monitor and Themis C measurements are time-shifted relative to MMS and Cluster using the solar wind velocity measurements and spacecraft separation along the X-axis. In panel e, the pale magenta curve highlights the B_Y changes discussed in the text for Themis C. Abbreviations: S/C - spacecraft.

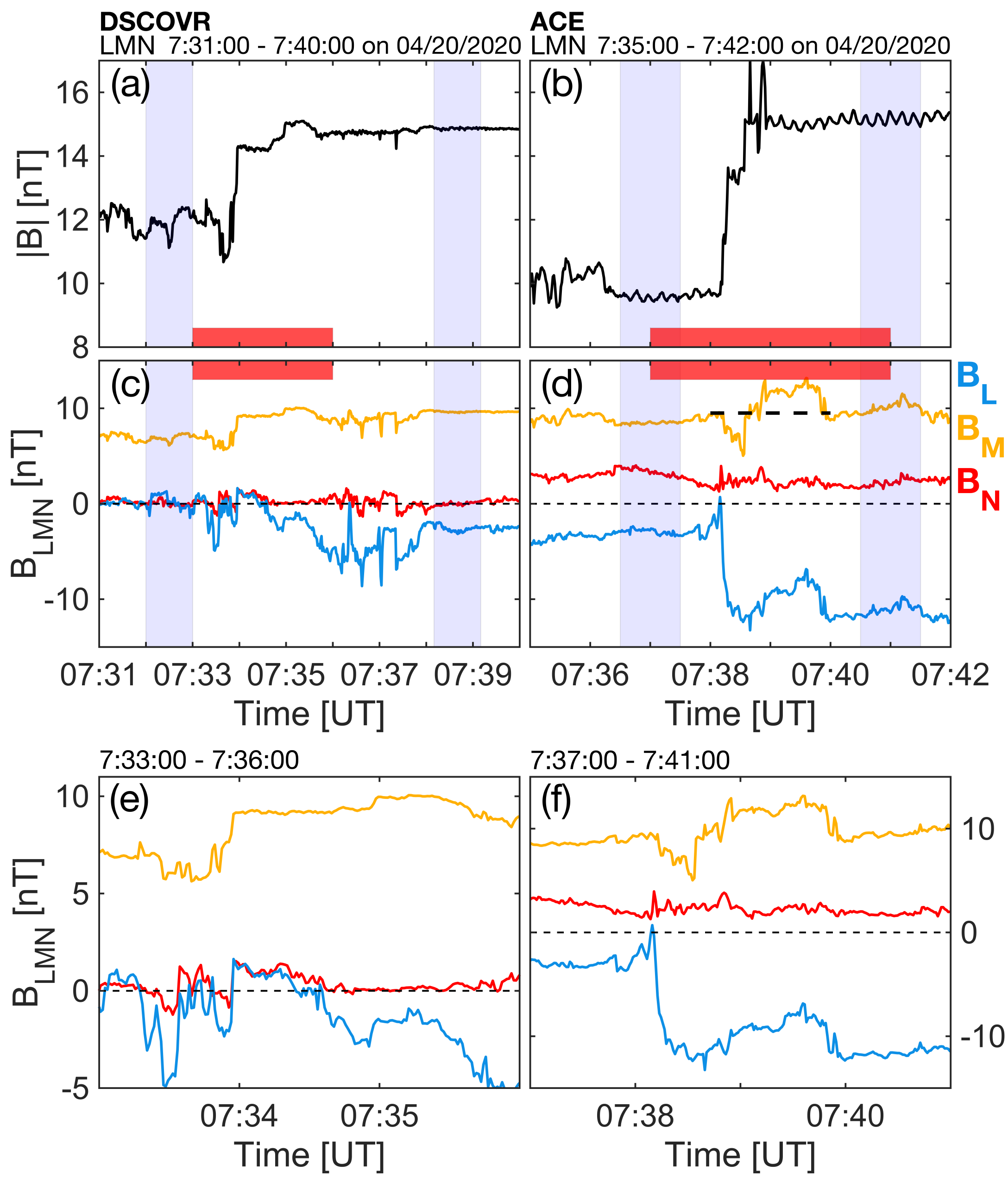

Figure 3. ICME front boundary on 20 April 2020 observed by the DSCOVR and ACE spacecraft. Panels show **(a-b)** the magnetic field magnitude, **(c-f)** the field components in the local LMN-coordinates. The blue shadings in panels a-d display the intervals that determine the normal directions. The red bars indicate the intervals shown in panels e-f.

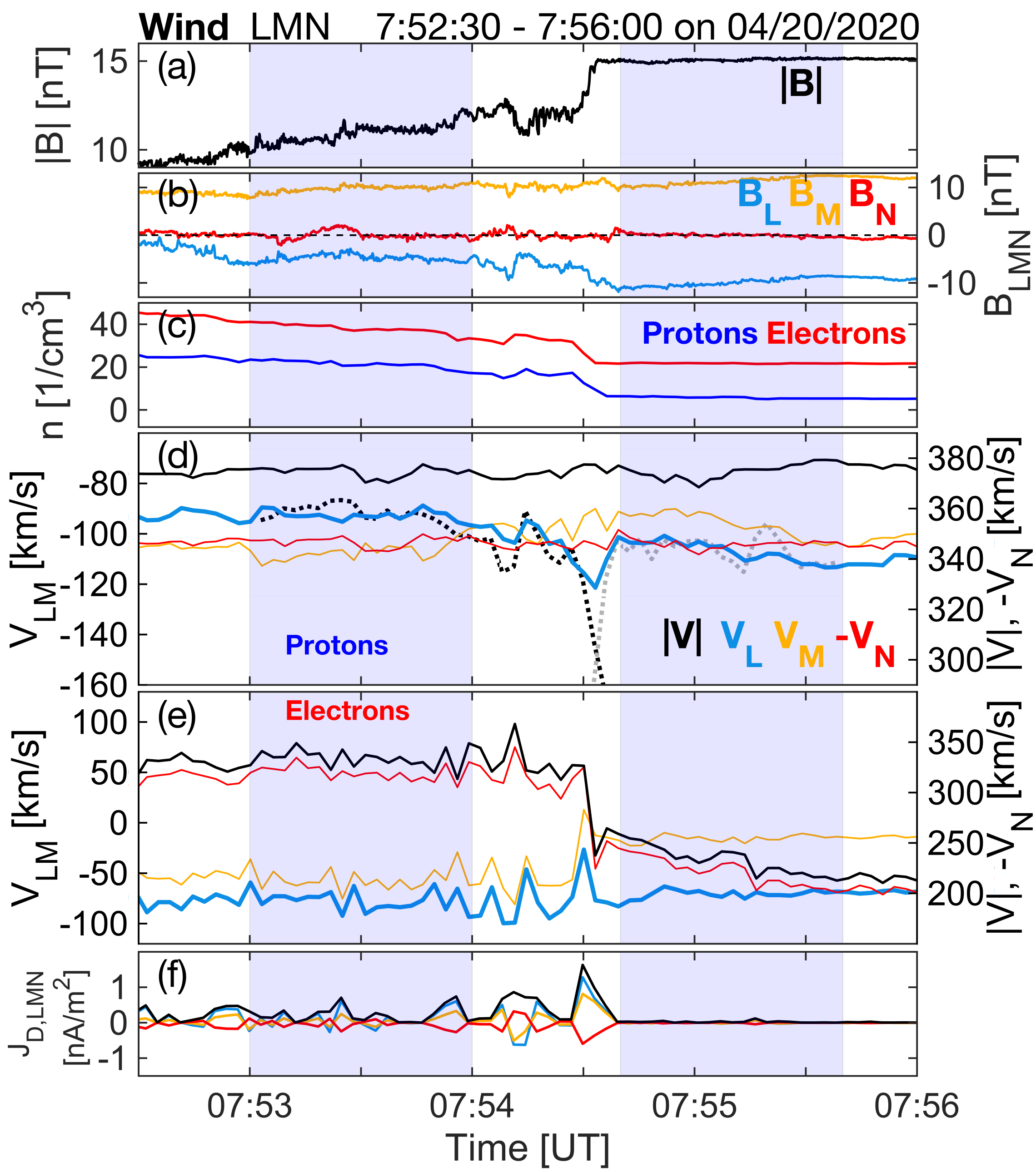

Figure 4. ICME front boundary on 20 April 2020 observed by the Wind spacecraft. Panels show **(a)** the magnetic field magnitude, **(b)** the field components in the local LMN-coordinates, **(c)** proton (blue) and electron (red) densities, **(d)** proton velocity and the Walén prediction of V_L from the sheath (ejecta) side on black (gray), **(e)** electron velocity, and **(f)** the diamagnetic current density ($\mathbf{J_D}$).

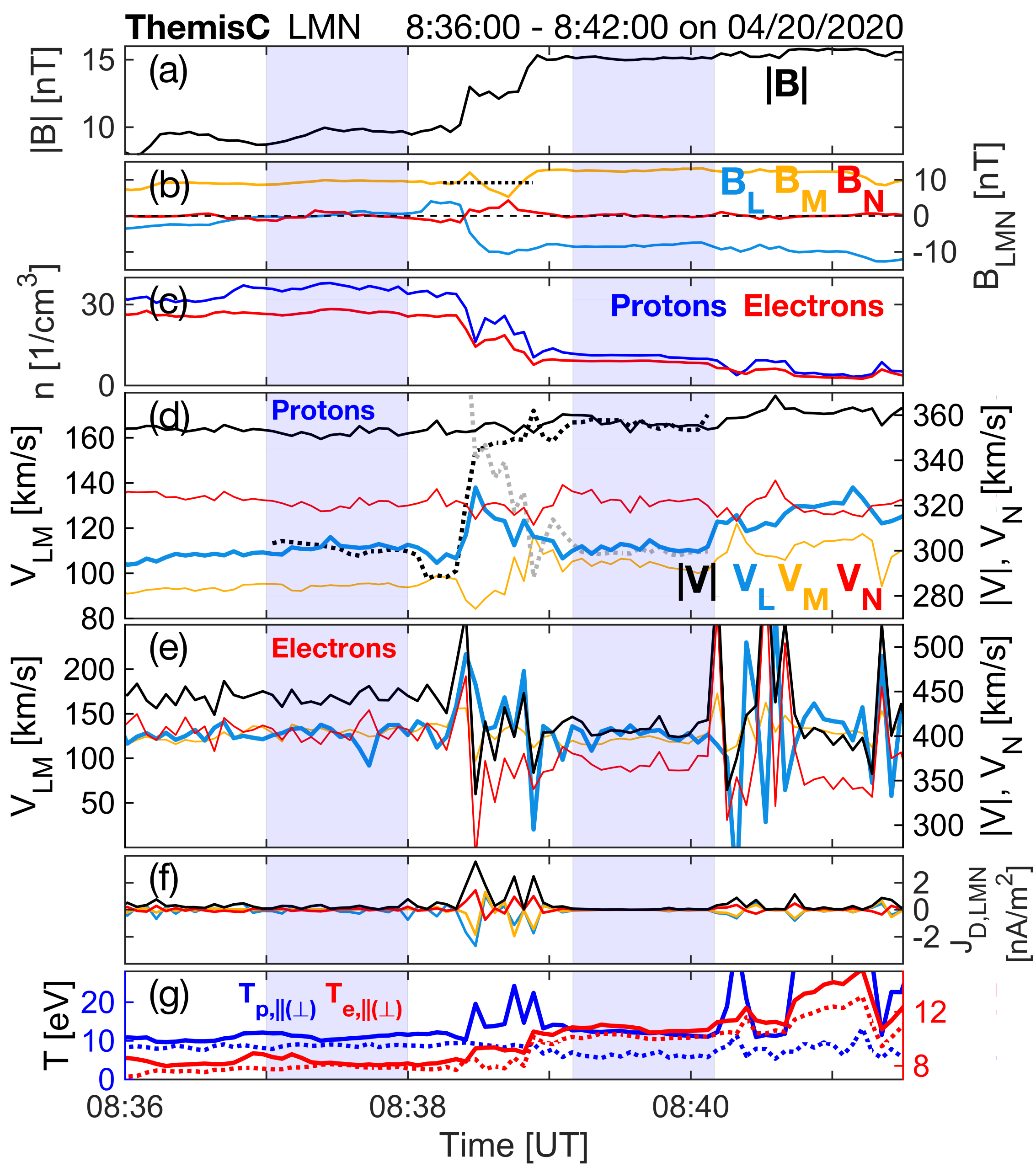

Figure 5. ICME front boundary on 20 April 2020 observed by the Themis C spacecraft. Panels show **(a)** the magnetic field magnitude, **(b)** the field components in the local LMN-coordinates, **(c)** proton (blue) and electron (red) densities, **(d)** proton velocity and the Walén prediction of V_L from the sheath (ejecta) side on black (gray), **(e)** electron velocity, **(f)** the diamagnetic current density, and **(g)** the parallel (||, solid) and perpendicular (⊥, dotted) proton and electron temperatures relative to the magnetic field.

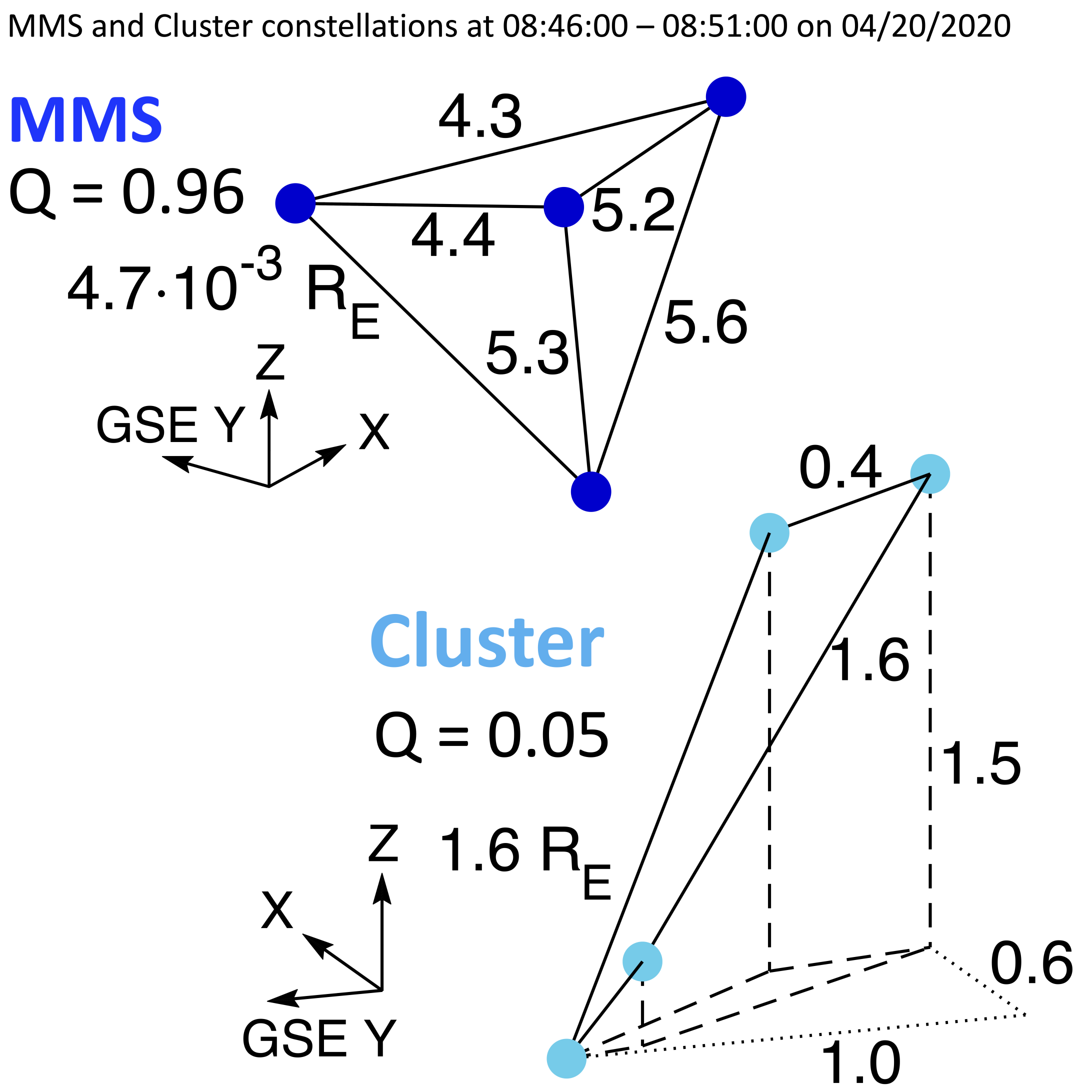

Figure 6. MMS and Cluster constellations during ICME front boundary passing on 20 April 2020. Constellation Q-factors quantifying the proximity to the perfect tetrahedron (Q=1) are shown.

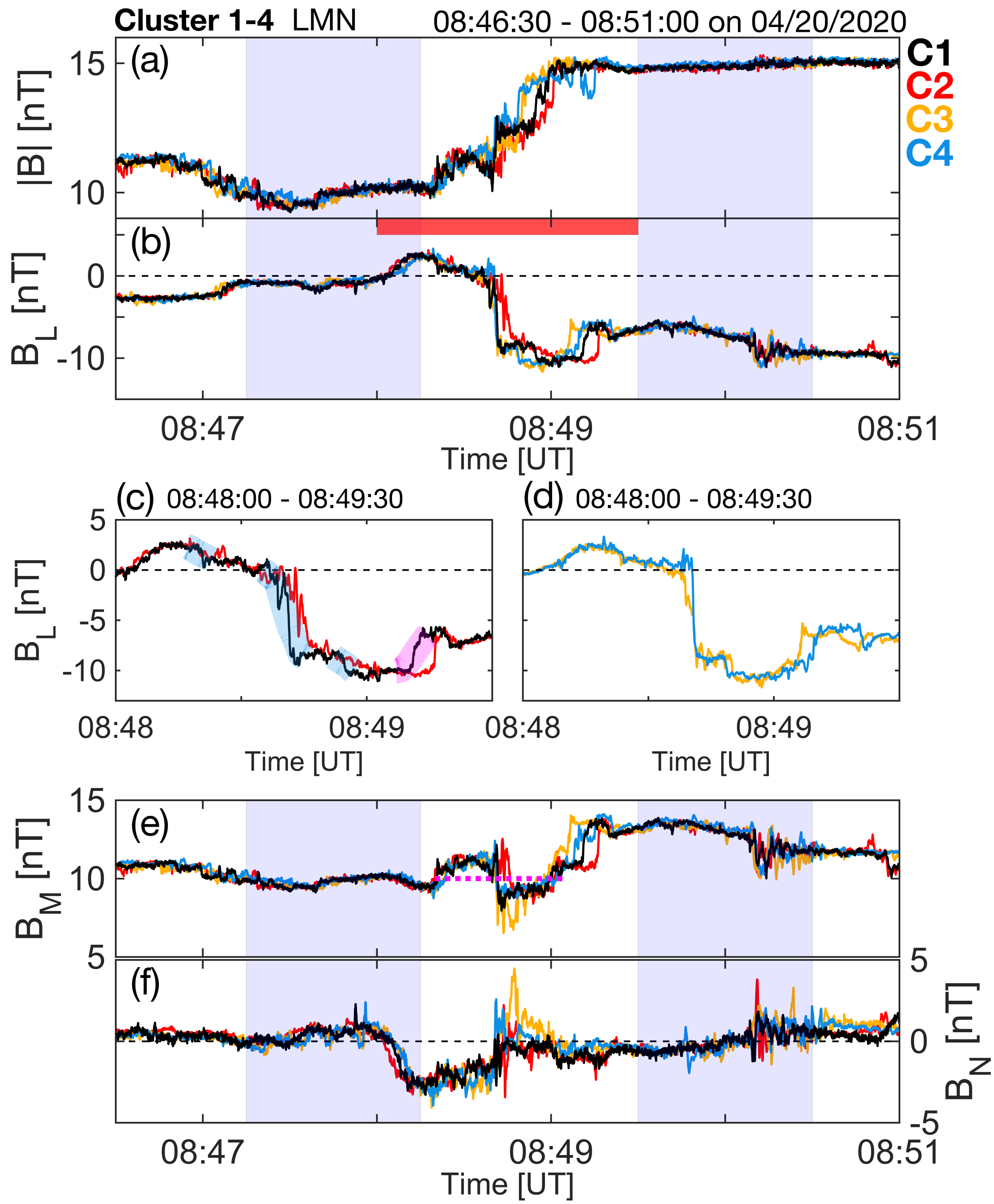

Figure 7. ICME front boundary on 20 April 2020 observed by the Cluster 1-4 spacecraft. Panels show **(a)** the magnetic field magnitude, and **(b-f)** the field components in the local LMN-coordinates. The blue shadings in panels a-b and e-f display the intervals that determine the normal directions. The red horizontal bar in panel a marks the interval shown in panels c-d. In panel c, the pale blue curves in panel c show the B_L-rotations aligned with field increases. The pale magenta curve marks the opposite rotation discussed in the text.

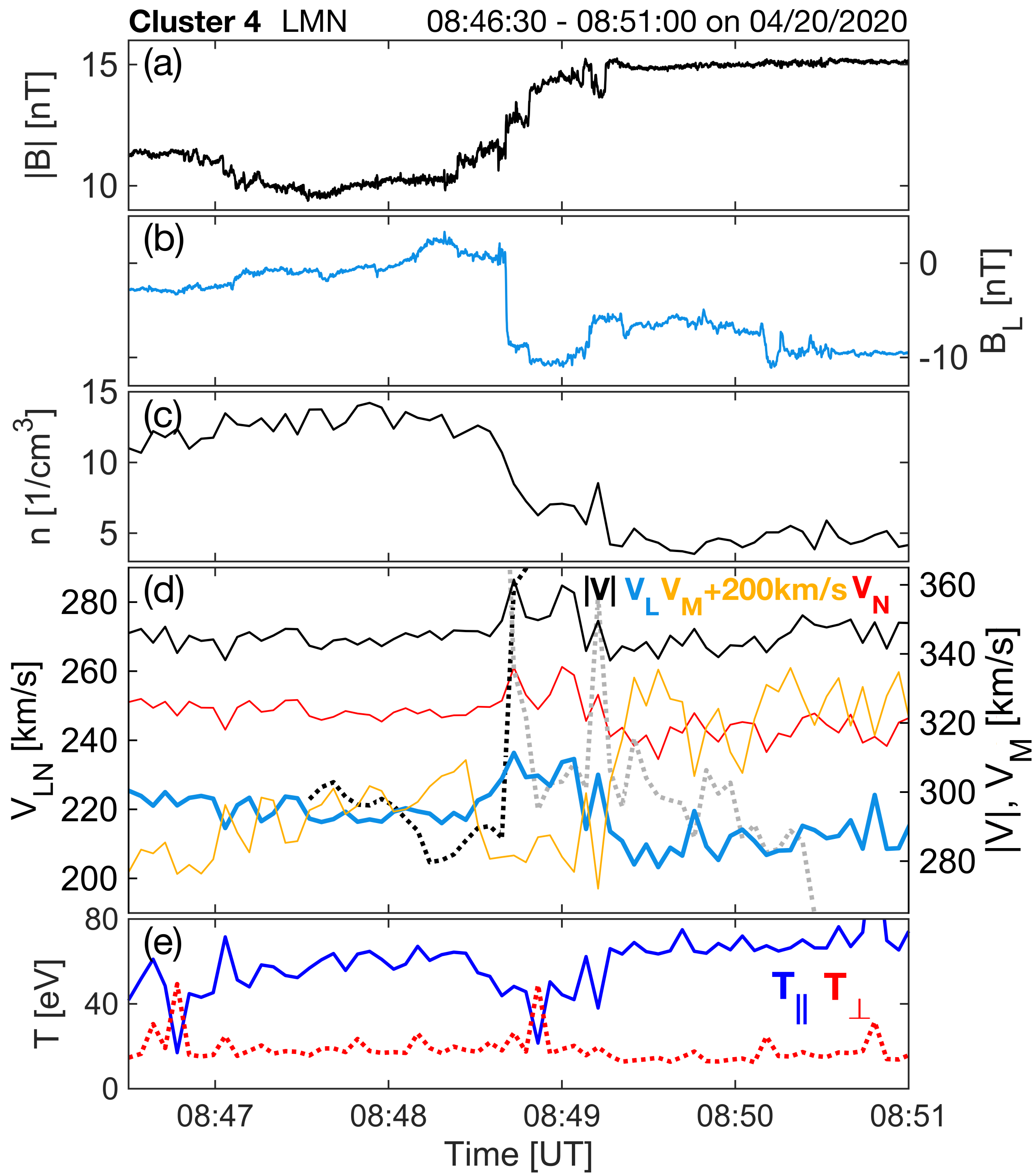

Figure 8. ICME front boundary on 20 April 2020 observed by Cluster 4. Panels show **(a)** the magnetic field magnitude, **(b-f)** B_L, **(c)** proton density, **(d)** velocity and the Walén prediction of V_L from the sheath (ejecta) side on black (gray), and **(e)** proton temperatures.

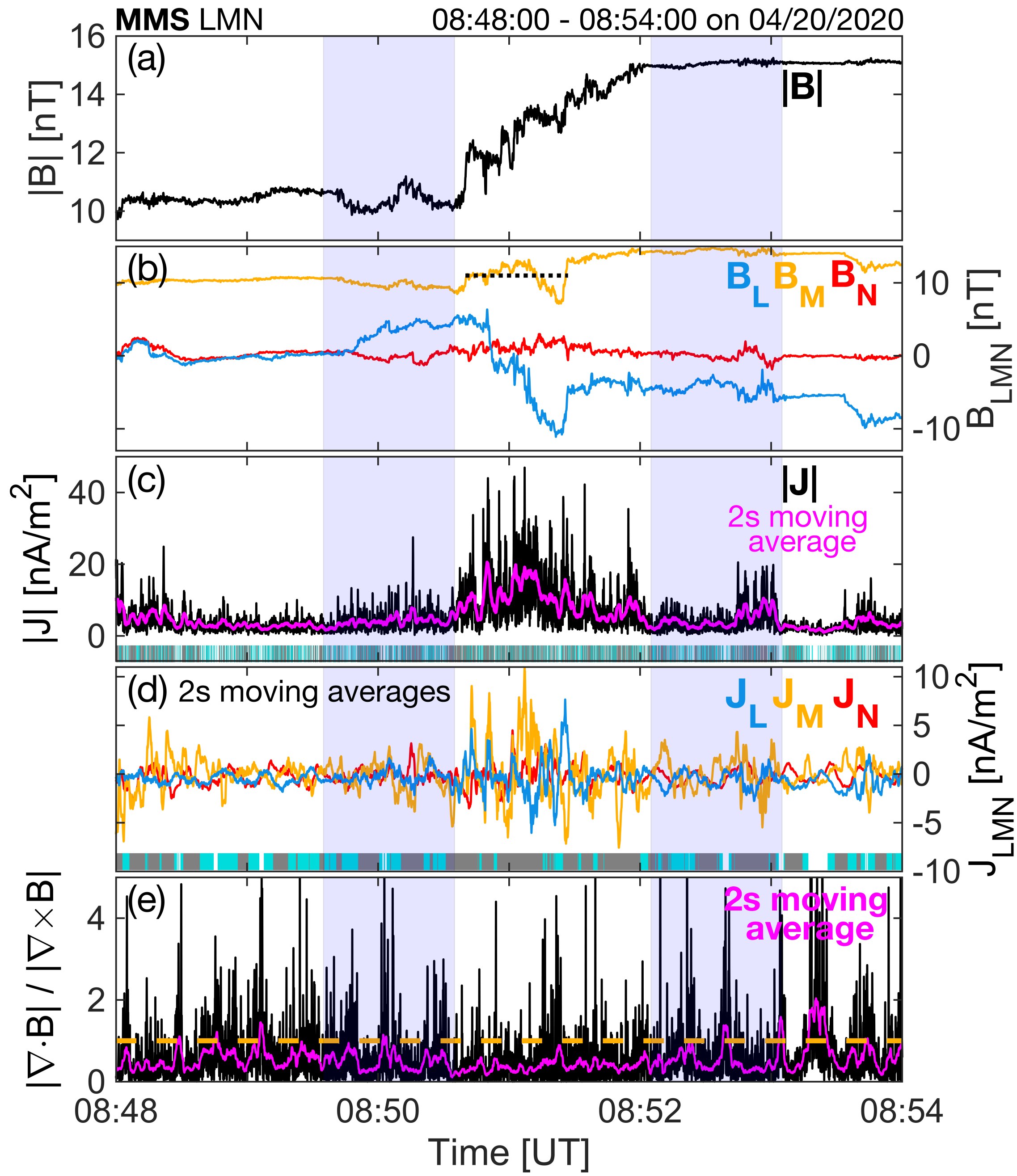

Figure 9. ICME front boundary on 20 April 2020 observed by MMS. Panels show **(a)** the magnetic field magnitude, **(b)** field components in the local LMN-coordinates, **(c)** the total current density, **(d)** 2 s moving averages of J_{LMN}-components, and **(e)** the magnetic field divergence-curl ratio, with the dashed orange line indicating the unity. In panel c the magenta gives the 2 s moving average of $|J|$. The gray (teal) bars at the bottom of panels c-d indicate the times when the divergence-curl ratio was below 0.5 (1), panel d showing the times for the average curve.

S/C	L GSE [X, Y, Z]	M	N	Magnetic Shear	$\lvert B_M/B_L \rvert$ Sheath Side - Ejecta Side	Magnetic Reconnection
DSCOVR	[0.30, -0.82, 0.49]	[0.11, -0.48, -0.87]	[0.95, 0.32, -0.06]	11°	61.82 - 5.59	No plasma data
ACE	[-0.45, 0.75, 0.48]	[-0.15, 0.47, -0.87]	[-0.88, -0.47, -0.10]	30°	2.90 - 0.93	No plasma data
Wind	[0.27, -0.69, 0.67]	[0.25, -0.62, -0.74]	[0.93, 0.37, 0.0]	15°	2.00 - 1.20	Ambiguous
Themis C	[-0.30, 0.85, 0.43]	[-0.28, 0.36, -0.89]	[-0.91, -0.39, 0.13]	35°	34.48 - 1.50	Yes
Cluster 4	[-0.61, 0.72, 0.33]	[-0.34, 0.14, -0.93]	[-0.72, -0.68, 0.16]	28°	21.78 - 1.71	Yes
MMS	[-0.23, 0.97, 0.10]	[-0.09, 0.07, -0.99]	[-0.97, -0.25, 0.07]	34°	3.36 - 3.19	No plasma data
Solar Orbiter	Shorter and less prevalent dip of $\lvert B \rvert$ at the ICME front than at the Earth's orbit; no plasma data					

Table 1. Parameters at the examined spacecraft during the ICME front boundary crossings. The table shows local LMN-coordinates given in GSE-coordinates, the magnetic shear angle across the boundary, the ratio between B_M- and B_L-component, and the occurrence of magnetic reconnection. The values are calculated using the intervals indicated by the blue shadings in the figures. Abbreviations: S/C - spacecraft.

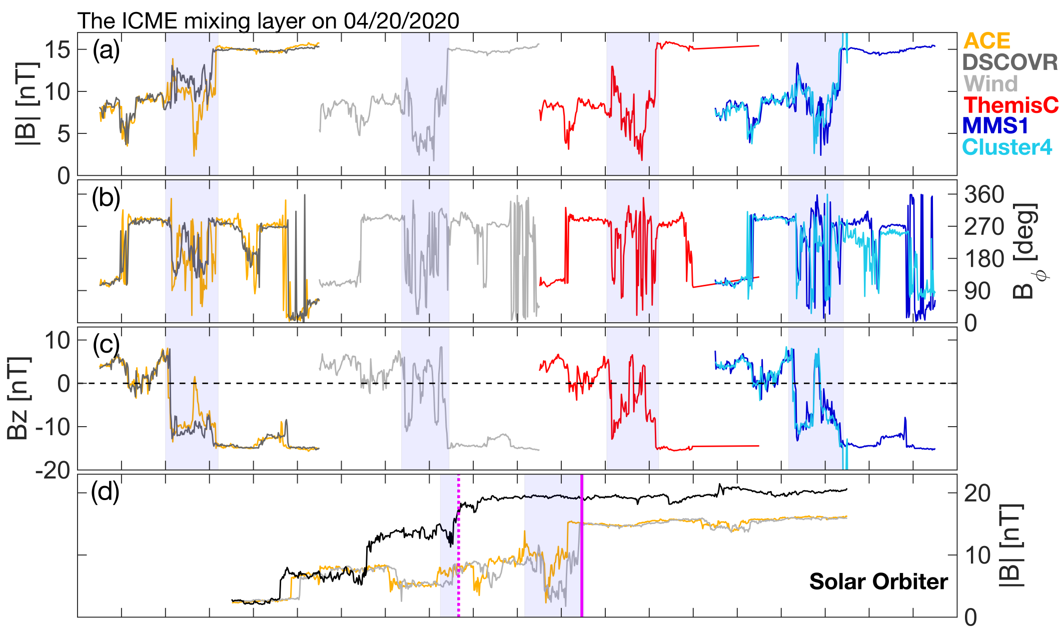

Figure 10. ICME mixing layer observed on 20 April 2020. Panels show **(a)** the magnetic field **magnitude**, **(b)** ϕ_B- and **(c)** B_Z-component from the spacecraft at the Earth's orbit, and **(d)** the field magnitude at ACE, Wind and Solar Orbiter at 1 min time-resolutions. The blue shadings indicate the mixing layer characterized by large rotations of ϕ_B and decreases of $\lvert B \rvert$. In panel d, vertical magenta lines show the ICME sheath-ejecta boundary. Spacecraft data is time-shifted arbitrarily **and** the distance between the ticks on the horizontal axis **corresponds to** 1 hour.

SWIFT Design Recommendations					
Mission Configuration	Number of Probes	Probe Separation [R_E]		Time-Resolution [s]	
		Radial	Transverse	Magnetic Field	Plasma
Baseline	1 hub at sub-L1 + 3 nodes at L1	$40 - 240$	$20 - 220$	≤ 1	≤ 1
Threshold	1 hub at sub-L1 + existing L1 assets	~ 150	~ 100	4	4

Table 2. Desired number of probes, their separations and instrument time-resolutions for Space Weather Investigation Frontier (SWIFT) mission (Akhavan-Tafti et al. 2023). Sub-L1 refers to sunward from the Lagrange L1 point. The transverse probe separation of the baseline configuration includes the minimum transverse probe separation ($\sim 20\,R_E$) and two times the maximum ($\sim 110\,R_E \rightarrow 220\,R_E$) analyzed in this study. The radial probe separation of the threshold configuration is given by the radial separation between Wind and Themis C.

REFERENCES

Akhavan-Tafti, M., Johnson, L., Sood, R., et al. 2023, Frontiers in Astronomy and Space Sciences, 10. https://www.frontiersin.org/articles/10.3389/fspas.2023.1185603/abstract

Al-Haddad, N., Lugaz, N., Poedts, S., et al. 2019, The Astrophysical Journal, 884, 179, doi: 10.3847/1538-4357/ab4126

Ala-Lahti, M., Dimmock, A. P., Pulkkinen, T. I., et al. 2021, Journal of Geophysical Research (Space Physics), 126, e29896, doi: 10.1029/2021JA029896

Ala-Lahti, M., Ruohotie, J., Good, S., Kilpua, E. K. J., & Lugaz, N. 2020, Journal of Geophysical Research (Space Physics), 125, e28002, doi: 10.1029/2020JA028002

Ala-Lahti, M. M., Kilpua, E. K. J., Dimmock, A. P., et al. 2018, Annales Geophysicae, 36, 793, doi: 10.5194/angeo-36-793-2018

Allen, R. C., Smith, E. J., Anderson, B. J., et al. 2022, Frontiers in Astronomy and Space Sciences, 9, 1002273, doi: 10.3389/fspas.2022.1002273

André, M., Li, W., Toledo-Redondo, S., et al. 2016, Geophysical Research Letters, 43, 6705, doi: 10.1002/2016GL069665

Angelopoulos, V. 2008, Space Science Reviews, 141, 5, doi: 10.1007/s11214-008-9336-1

Borovsky, J. E. 2018, Journal of Atmospheric and Solar-Terrestrial Physics, 177, 2, doi: 10.1016/j.jastp.2017.03.014

Burch, J. L., Moore, T. E., Torbert, R. B., & Giles, B. L. 2016, Space Science Reviews, 199, 5, doi: 10.1007/s11214-015-0164-9

Burt, J., & Smith, B. 2012, in 2012 IEEE Aerospace Conference, 1–13, doi: 10.1109/AERO.2012.6187025

Che, H., Zank, G. P., Benz, A. O., Tang, B., & Crawford, C. 2021, The Astrophysical Journal, 908, 72, doi: 10.3847/1538-4357/abcf29

Chian, A. C. L., & Muñoz, P. R. 2011, The Astrophysical Journal Letters, 733, L34, doi: 10.1088/2041-8205/733/2/L34

Dai, L. 2018, Journal of Geophysical Research (Space Physics), 123, 7332, doi: 10.1029/2018JA025251

Dasso, S., Mandrini, C. H., Démoulin, P., & Luoni, M. L. 2006, Astronomy and Astrophysics, 455, 349, doi: 10.1051/0004-6361:20064806

Davies, E. E., Möstl, C., Owens, M. J., et al. 2021, Astronomy & Astrophysics, 656, A2, doi: 10.1051/0004-6361/202040113

Denton, R. E., Sonnerup, B. U. Ö., Hasegawa, H., et al. 2016, Journal of Geophysical Research (Space Physics), 121, 9880, doi: 10.1002/2016JA023323

Di Matteo, S., & Sivadas, N. 2022, Frontiers in Astronomy and Space Sciences, 9, 333, doi: 10.3389/fspas.2022.1060072

Dunlop, M. W., Balogh, A., Glassmeier, K. H., & Robert, P. 2002, Journal of Geophysical Research (Space Physics), 107, 1384, doi: 10.1029/2001JA005088

Eastwood, J. P., Shay, M. A., Phan, T. D., & Øieroset, M. 2010, Physical Review Letters, 104, 205001, doi: 10.1103/PhysRevLett.104.205001

Eastwood, J. P., Mistry, R., Phan, T. D., et al. 2018, Geophysical Research Letters, 45, 4569, doi: 10.1029/2018GL077670

Eastwood, J. P., Stawarz, J. E., Phan, T. D., et al. 2021, Astronomy & Astrophysics, 656, A27, doi: 10.1051/0004-6361/202140949

Enžl, J., Šafránková, J., Němeček, Z., & Přech, L. 2017, The Astrophysical Journal, 851, 86, doi: 10.3847/1538-4357/aa98e0

Eriksson, S., Newman, D. L., Lapenta, G., & Angelopoulos, V. 2014, Plasma Physics and Controlled Fusion, 56, 064008, doi: 10.1088/0741-3335/56/6/064008

Eriksson, S., Gosling, J. T., Phan, T. D., et al. 2009, Journal of Geophysical Research (Space Physics), 114, A07103, doi: 10.1029/2008JA013990

Eriksson, S., Lapenta, G., Newman, D. L., et al. 2015, The Astrophysical Journal, 805, 43, doi: 10.1088/0004-637X/805/1/43

Eriksson, S., Swisdak, M., Weygand, J. M., et al. 2022, The Astrophysical Journal, 933, 181, doi: 10.3847/1538-4357/ac73f6

Escoubet, C. P., Schmidt, R., & Goldstein, M. L. 1997, Space Science Reviews, 79, 11, doi: 10.1023/A:1004923124586

Farrugia, C. J., Vasquez, B. J., Lugaz, N., et al. 2023, The Astrophysical Journal, 953, 15, doi: 10.3847/1538-4357/acdcf7

Fox, N. J., Velli, M. C., Bale, S. D., et al. 2016, Space Science Reviews, 204, 7, doi: 10.1007/s11214-015-0211-6

Freiherr von Forstner, J. L., Dumbović, M., Möstl, C., et al. 2021, Astronomy & Astrophysics, 656, A1, doi: 10.1051/0004-6361/202039848

Fu, H. S., Vaivads, A., Khotyaintsev, Y. V., et al. 2017, Geophysical Research Letters, 44, 37, doi: 10.1002/2016GL071787

George, D. E., & Jahn, J.-M. 2020, Journal of Geophysical Research (Space Physics), 125, e27339, doi: 10.1029/2019JA027339

Good, S. W., Ala-Lahti, M., Palmerio, E., Kilpua, E. K. J., & Osmane, A. 2020, The Astrophysical Journal, 893, 110, doi: 10.3847/1538-4357/ab7fa2

Good, S. W., Forsyth, R. J., Eastwood, J. P., & Möstl, C. 2018, Solar Physics, 293, 52, doi: 10.1007/s11207-018-1264-y

Good, S. W., Forsyth, R. J., Raines, J. M., et al. 2015, The Astrophysical Journal, 807, 177, doi: 10.1088/0004-637X/807/2/177

Gosling, J. T., Eriksson, S., & Schwenn, R. 2006a, Journal of Geophysical Research (Space Physics), 111, A10102, doi: 10.1029/2006JA011863

Gosling, J. T., Eriksson, S., Skoug, R. M., McComas, D. J., & Forsyth, R. J. 2006b, The Astrophysical Journal, 644, 613, doi: 10.1086/503544

Gosling, J. T., & Phan, T. D. 2013, The Astrophysical Journal Letters, 763, L39, doi: 10.1088/2041-8205/763/2/L39

Gosling, J. T., Skoug, R. M., McComas, D. J., & Smith, C. W. 2005, Journal of Geophysical Research (Space Physics), 110, A01107, doi: 10.1029/2004JA010809

Gosling, J. T., & Szabo, A. 2008, Journal of Geophysical Research (Space Physics), 113, A10103, doi: 10.1029/2008JA013473

Haaland, S., Sonnerup, B. U. Ö., Dunlop, M. W., et al. 2004, Geophysical Research Letters, 31, L10804, doi: 10.1029/2004GL020001

Hesse, M., Norgren, C., Tenfjord, P., et al. 2018, Physics of Plasmas, 25, 122902, doi: 10.1063/1.5054100

Heyn, M. F., Biernat, H. K., Semenov, V. S., & Kubyshkin, I. V. 1985, Journal of Geophysical Research, 90, 1781, doi: 10.1029/JA090iA02p01781

Higashimori, K., & Hoshino, M. 2015, Journal of Geophysical Research (Space Physics), 120, 1803, doi: 10.1002/2014JA020544

Huang, C., Lu, Q., Wang, R., et al. 2017, The Astrophysical Journal, 835, 245, doi: 10.3847/1538-4357/835/2/245

Huttunen, K., & Koskinen, H. 2004, Annales Geophysicae, 22, 1729, doi: 10.5194/angeo-22-1729-2004

Huttunen, K. E. J., Bale, S. D., Phan, T. D., Davis, M., & Gosling, J. T. 2007, Journal of Geophysical Research (Space Physics), 112, A01102, doi: 10.1029/2006JA011836

Huttunen, K. E. J., Bale, S. D., & Salem, C. 2008, Annales Geophysicae, 26, 2701, doi: 10.5194/angeo-26-2701-2008

Huttunen, K. E. J., Koskinen, H. E. J., & Schwenn, R. 2002, Journal of Geophysical Research (Space Physics), 107, 1121, doi: 10.1029/2001JA900171

Innocenti, M. E., Goldman, M., Newman, D., Markidis, S., & Lapenta, G. 2015, The Astrophysical Journal Letters, 810, L19, doi: 10.1088/2041-8205/810/2/L19

Jiang, L., & Lu, S. 2021, AIP Advances, 11, 015001, doi: 10.1063/5.0037770

Kilpua, E., Koskinen, H. E. J., & Pulkkinen, T. I. 2017, Living Reviews in Solar Physics, 14, 5, doi: 10.1007/s41116-017-0009-6

Kilpua, E. K. J., Isavnin, A., Vourlidas, A., Koskinen, H. E. J., & Rodriguez, L. 2013, Annales Geophysicae, 31, 1251, doi: 10.5194/angeo-31-1251-2013

Kilpua, E. K. J., Fontaine, D., Moissard, C., et al. 2019, Space Weather, 17, 1257, doi: 10.1029/2019SW002217

Kilpua, E. K. J., Good, S. W., Dresing, N., et al. 2021, Astronomy & Astrophysics, 656, A8, doi: 10.1051/0004-6361/202140838

Knetter, T., Neubauer, F. M., Horbury, T., & Balogh, A. 2004, Journal of Geophysical Research (Space Physics), 109, A06102, doi: 10.1029/2003JA010099

Lapenta, G., Goldman, M. V., Newman, D. L., & Markidis, S. 2017, Plasma Physics and Controlled Fusion, 59, 014019, doi: 10.1088/0741-3335/59/1/014019

Lavraud, B., Ruffenach, A., Rouillard, A. P., et al. 2014, Journal of Geophysical Research (Space Physics), 119, 26, doi: 10.1002/2013JA019154

Le, A., Egedal, J., Ng, J., et al. 2014, Physics of Plasmas, 21, 012103, doi: 10.1063/1.4861871

Lepping, R. P., Acũna, M. H., Burlaga, L. F., et al. 1995, Space Science Reviews, 71, 207, doi: 10.1007/BF00751330

Lin, Y., & Lee, L. C. 1993, Space Science Reviews, 65, 59, doi: 10.1007/BF00749762

Liu, C., Feng, X., Guo, J., & Fu, H. 2021, Astrophysics and Space Science, 366, 2, doi: 10.1007/s10509-020-03910-6

Lugaz, N., Farrugia, C. J., Winslow, R. M., et al. 2018, The Astrophysical Journal Letters, 864, L7, doi: 10.3847/2041-8213/aad9f4

Lugaz, N., Salman, T. M., Zhuang, B., et al. 2022, The Astrophysical Journal, 929, 149, doi: 10.3847/1538-4357/ac602f

Manchester, W., Kilpua, E. K. J., Liu, Y. D., et al. 2017, Space Science Reviews, 212, 1159, doi: 10.1007/s11214-017-0394-0

Mistry, R., Eastwood, J. P., Haggerty, C. C., et al. 2016, Physical Review Letters, 117, 185102, doi: 10.1103/PhysRevLett.117.185102

Mistry, R., Eastwood, J. P., & Hietala, H. 2015a, Journal of Geophysical Research (Space Physics), 120, 30, doi: 10.1002/2014JA020465

Mistry, R., Eastwood, J. P., Phan, T. D., & Hietala, H. 2015b, Geophysical Research Letters, 42, 10,513, doi: 10.1002/2015GL066820

Müller, D., Marsden, R. G., St. Cyr, O. C., Gilbert, H. R., & Solar Orbiter Team. 2013, Solar Physics, 285, 25, doi: 10.1007/s11207-012-0085-7

Nykyri, K., Ma, X., Burkholder, B., et al. 2023, Frontiers in Astronomy and Space Sciences, 10, doi: 10.3389/fspas.2023.1179344

Ogilvie, K. W., Chornay, D. J., Fritzenreiter, R. J., et al. 1995, Space Science Reviews, 71, 55, doi: 10.1007/BF00751326

O'Kane, J., Green, L. M., Davies, E. E., et al. 2021, Astronomy & Astrophysics, 656, L6, doi: 10.1051/0004-6361/202140622

Owen, C. J., Foster, A. C., Bruno, R., et al. 2021, Astronomy & Astrophysics, 656, L8, doi: 10.1051/0004-6361/202140944

Palmerio, E., Kilpua, E. K. J., & Savani, N. P. 2016, Annales Geophysicae, 34, 313, doi: 10.5194/angeo-34-313-2016

Palmerio, E., Nieves-Chinchilla, T., Kilpua, E. K. J., et al. 2021, Journal of Geophysical Research (Space Physics), 126, e2021JA029770, doi: 10.1029/2021JA029770

Paschmann, G., Papamastorakis, I., Baumjohann, W., et al. 1986, Journal of Geophysical Research, 91, 11099, doi: 10.1029/JA091iA10p11099

Peng, F. Z., Fu, H. S., Cao, J. B., et al. 2017, Journal of Geophysical Research (Space Physics), 122, 6349, doi: 10.1002/2016JA023666

Petschek, H. E. 1964, in NASA Special Publication, Vol. 50, 425

Phan, T. D., Paschmann, G., & Sonnerup, B. U. Ö. 1996, Journal of Geophysical Reserach, 101, 7817, doi: 10.1029/95JA03751

Phan, T. D., Gosling, J. T., Davis, M. S., et al. 2006, Nature, 439, 175, doi: 10.1038/nature04393

Phan, T. D., Eastwood, J. P., Cassak, P. A., et al. 2016, Geophysical Research Letters, 43, 6060, doi: 10.1002/2016GL069212

Phan, T. D., Bale, S. D., Eastwood, J. P., et al. 2020, The Astrophysical Journal Supplement Series, 246, 34, doi: 10.3847/1538-4365/ab55ee

Robert, P., Roux, A., Harvey, C. C., et al. 1998, ISSI Scientific Reports Series, 1, 323

Ruffenach, A., Lavraud, B., Owens, M. J., et al. 2012, Journal of Geophysical Research (Space Physics), 117, A09101, doi: 10.1029/2012JA017624

Ruffenach, A., Lavraud, B., Farrugia, C. J., et al. 2015, Journal of Geophysical Research (Space Physics), 120, 43, doi: 10.1002/2014JA020628

Salman, T. M., Winslow, R. M., & Lugaz, N. 2020, Journal of Geophysical Research (Space Physics), 125, e27084, doi: 10.1029/2019JA027084

Sasunov, Y. L., Semenov, V. S., Heyn, M. F., Kubyshkin, I. V., & Biernat, H. K. 2012, Geophysical Research Letters, 39, L06104, doi: 10.1029/2012GL051273

Scolini, C., Winslow, R. M., Lugaz, N., & Poedts, S. 2021, The Astrophysical Journal Letters, 916, L15, doi: 10.3847/2041-8213/ac0d58

Semenov, V. S., Hejn, M. F., & Kubyshkin, I. V. 1983, Astronomicheskii Zhurnal, 60, 1138

Siscoe, G., & Odstrcil, D. 2008, Journal of Geophysical Research (Space Physics), 113, A00B07, doi: 10.1029/2008JA013142

Sivadas, N., & Sibeck, D. G. 2022, Frontiers in Astronomy and Space Sciences, 9, 924976, doi: 10.3389/fspas.2022.924976

Sonnerup, B. U. Ö., & Scheible, M. 1998, ISSI Scientific Reports Series, 1, 185

Sonnerup, B. U. O., Paschmann, G., Papamastorakis, I., et al. 1981, Journal of Geophysical Research, 86, 10049, doi: 10.1029/JA086iA12p10049

Stone, E. C., Frandsen, A. M., Mewaldt, R. A., et al. 1998, Space Science Reviews, 86, 1, doi: 10.1023/A:1005082526237

Teh, W. L., Sonnerup, B. U. Ö., Hu, Q., & Farrugia, C. J. 2009, Annales Geophysicae, 27, 807, doi: 10.5194/angeo-27-807-2009

Vasquez, B. J., Abramenko, V. I., Haggerty, D. K., & Smith, C. W. 2007, Journal of Geophysical Research (Space Physics), 112, A11102, doi: 10.1029/2007JA012504

Vörös, Z., Varsani, A., Yordanova, E., et al. 2021, Journal of Geophysical Research (Space Physics), 126, e29415, doi: 10.1029/2021JA029415

Vourlidas, A., Lynch, B. J., Howard, R. A., & Li, Y. 2013, Solar Physics, 284, 179, doi: 10.1007/s11207-012-0084-8

Walén, C. 1944, Arkiv for Matematik, Astronomi och Fysik, 30A, 1

Walia, N. K., Seki, K., & Amano, T. 2022, Journal of Geophysical Research (Space Physics), 127, e30066, doi: 10.1029/2021JA030066

Walsh, B. M., Bhakyapaibul, T., & Zou, Y. 2019, Journal of Geophysical Research (Space Physics), 124, 3291, doi: 10.1029/2019JA026507

Wang, R., Wang, S., Lu, Q., et al. 2022, Nature Astronomy, doi: 10.1038/s41550-022-01818-5

Wei, F., Liu, R., Fan, Q., & Feng, X. 2003, Journal of Geophysical Research (Space Physics), 108, 1263, doi: 10.1029/2002JA009511

Wilder, F. D., Ergun, R. E., Eriksson, S., et al. 2017, Physical Review Letters, 118, 265101, doi: 10.1103/PhysRevLett.118.265101

Zurbuchen, T. H., & Richardson, I. G. 2006, Space Science Reviews, 123, 31, doi: 10.1007/s11214-006-9010-4